Chirped-Pulse Interferometry:

Classical dispersion cancellation and analogues of two-photon quantum interference

by

Jonathan Lavoie

A thesis
presented to the University of Waterloo
in fulfillment of the
thesis requirement for the degree of
Master of Science
in
Physics

Waterloo, Ontario, Canada, 2009

I hereby declare that I am the sole author of this thesis. This is a true copy of the thesis, including any required final revisions, as accepted by my examiners.

I understand that my thesis may be made electronically available to the public.

Abstract

Interference has long been used for precision measurement of path-length changes. Since the advent of the laser, interference has become one of the most versatile tools in metrology. Specifically, ultra-short laser pulses allow unprecedented resolution in absolute length measurements. While ultra-short laser pulses lead to high resolution, for example in white-light interferometry, they are very susceptible to dispersion.

Quantum resources have been proposed to overcome some of the problems related to distortions in the interferometric signal. For example, the Hong-Ou-Mandel (HOM) interferometer relies on frequency-entangled photon pairs and features automatic even-order dispersion cancellation and high interference visibility resilient to unbalanced loss. Quantum-OCT is a technique based on HOM interferometry, that promises to overcome Optical Coherence Tomography (OCT) a classical imaging technique based on low coherence light. Furthermore, straightforward modifications of the HOM interferometer can display several different interferometric signals, including the HOM peak, quantum beating, and phase super-resolution. However, the quantum resources required are hard to produce and dim, leading to long integration times and single-photon counting.

In this thesis, we introduce the theory behind Chirped-Pulse Interferometry (CPI), a new technique that combines all the advantages of Q-OCT, including even-order dispersion cancellation, but without the need for any quantum resources. We then experimentally implement CPI and demonstrate all the important characteristics shared by the HOM interferometer, but at dramatically larger signal levels. We show how CPI can be used to measure dispersion cancelled axial profiles of an optical sample and show the improvement in resolution over white-light interferometry. Finally, we show that by modifying CPI in analogous ways to HOM, CPI can also be made to produce interferometric signal identical to the HOM peak, quantum beating, and phase super-resolution.

Acknowledgements

Firstly, I would like to thank Kevin Resch for his effective supervision. I feel lucky to have had my chance in his group, and more than happy to stay around for the PhD. I would like to thank my friends in the Quantum Optics Group: Devon, Deny and Kurt, for their unconditional help in the lab, and helpful suggestions for my thesis. I should also thank Rainer Kaltenbaek, to whom I owe the success of my Master's.

On behalf of my colleagues, we thank D. Strickland for sharing expertise on pulse compression techniques, K. Bizheva and G. Weihs and C. Couteau for discussions, but also for loaning equipment and technical assistance. We thank J. Sanderson, J. Lundeen, M. Mitchell, J. Gambetta, A. White and A. Steinberg for comments on our work. We acknowledge financial support from NSERC and CFI. I personally acknowledge financial support from the Bell Family Fund.

The Institute for Quantum Computing is an outstanding place for studying and I thank all the members and direction to have developed and refined the establishment. I am also thankful toward the staff of IQC, which makes our life substantially easier.

As perfect the workplace could be, in Waterloo, one cannot psychologically survive without friends. I thank Mathhias, Tobias and Rainer for the good time we had in the civilized world. Also, thanks to the crowd of the International Student's Pub Night, especially to have accepted me at their table, before the time that Quebec becomes a nation.

I would like to acknowledge the precious support of my family and parents. A special thank to my uncle, and friend Jean for his interest in my studies and encouragements.

Finally, I thank the members of my committee, Kevin Resch, Donna Strickland and Norbert Lütkenhaus for valuable discussions and comments. I also thank Thomas Jennewein to have accepted to be part of the final examining committee.

Contents

List of Figures

Chapter 1

Background

1.1 Ultrashort Laser Pulses

Ultrashort light pulses are electromagnetic wave packets emitted, for example, from a mode-locked laser, oscillating at the carrier frequency ω_l. Femtosecond ($fs = 10^{-15}$ s) pulses have very short coherence lengths and are therefore a valuable resource in low coherence interferometry for precise absolute position measurements. For example, a 10 fs long laser pulse corresponds to just 3 μm in vacuum.

Before we discuss chirped-pulse interferometry, we will define and describe a number of important concepts. We will overview some fundamental characteristics of ultrafast laser pulses and describe the effects of dispersive materials on their properties. We will describe two types of interferometers, white-light interferometry and Hong-Ou-Mandel (HOM), and how their characteristic differ once dispersion is considered. These concepts will all be revisited in the subsequent chapters.

1.1.1 Essential Pulse Characteristics

Light pulses can be described by the time and space dependent electric field. In this subsection, we summarize the essential notations and definitions used to describe the electromagnetic wave packet, in its complex representation. While a general description of the electric field requires $\overrightarrow{E}(x, y, z, t)$, it suffices, for our purposes, to consider the simplified

field with its temporal dependance $E(t)$. A complete description could also be given in the frequency domain. For convenience, we use complex representation, but should keep in mind that the measured quantities are real. The complex electric field, $E(t)$, and the complex spectrum of the field $E(\Omega)$ are related through the complex Fourier transform ($\mathfrak{F}$) and inverse Fourier transform ($\mathfrak{F}^{-1}$) :

$$E(\Omega) = \mathfrak{F}\{E(t)\} = \int_{-\infty}^{\infty} E(t)e^{-i\omega t}dt = |\mathcal{E}(\Omega)|e^{i\phi(\Omega)} \tag{1.1}$$

$$E(t) = \mathfrak{F}^{-1}\{E(\Omega)\} = \frac{1}{2\pi}\int_{-\infty}^{\infty} \mathcal{E}(\Omega)e^{i\omega t}d\Omega \tag{1.2}$$

In the expression (1.1), $|\mathcal{E}(\Omega)|$ denotes the spectral amplitude and $\phi(\Omega)$ is the spectral phase. Experimentally, one can obtain the spectral intensity of the light ($S(\Omega) \propto |\mathcal{E}(\Omega)|^2$) using a spectrometer.

In general, the complex electric field $E(t)$ can also be represented by a real field envelope $\mathcal{E}(t)$ and a phase term [1]:

$$E(t) = \frac{1}{2}\mathcal{E}(t)e^{i\Gamma(t)} \tag{1.3}$$

When this expression is summed with its complex conjugate (c.c), the new quantity corresponds to the real electric field. The phase term in expression (1.3) can be decomposed using a carrier frequency ω_l and a time-dependant phase: $\Gamma(t) = \omega_l t + \psi(t)$. The electric field is thus rewritten as:

$$E(t) = \frac{1}{2}\mathcal{E}(t)e^{i(\omega_l t+\psi(t))} \tag{1.4}$$

The phase function $\psi(t)$ has an important physical meaning. It tells us the frequency evolution of the pulse in time. The pulse instantaneous frequency, $\omega(t)$, is defined as:

$$\omega(t) = \omega_l + \frac{d}{dt}\psi(t) \tag{1.5}$$

One can see that for $\frac{d}{dt}\psi(t) = b = \text{const.}$, the carrier frequency is just shifted to $\omega_l + b$. For $\frac{d}{dt}\psi(t) = f(t)$, the carrier frequency varies with time and the corresponding pulse is said to be frequency modulated, or chirped. Depending on the second derivative of $\psi(t)$, the instantaneous frequency will decrease or increase along the pulse, giving rise to a down-chirp or a up-chirp, respectively. Figure 1.1 is an example of an up-chirped electric field, shown temporally.

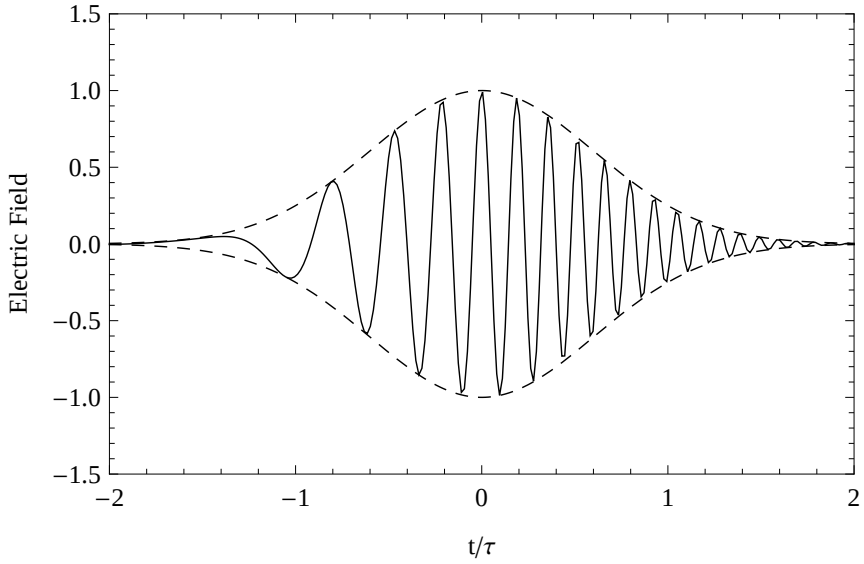

Figure 1.1: Electric field of a frequency modulated (chirped) Gaussian pulse $E(t) = \exp\left[-2\ln 2(t/\tau)^2\right]\cos\left(\omega_l t + \beta t^2\right)$. The full width of half maximum of the intensity envelope was chosen as $\tau = 10\pi/\omega_l$ and the chirp parameter $\beta = 10/\tau^2$

In the frequency domain, the group delay is an analogue to the instantaneous frequency. With the electric field expressed in the frequency domain as (1.1), the group delay is the derivative of the spectral phase:

$$\tau_g(\Omega) = \frac{d\phi}{d\Omega}. \tag{1.6}$$

If we expand the spectral phase in a Taylor series:

$$\phi(\omega) = \phi_l + \phi_1\Omega + \frac{1}{2}\phi_2\Omega^2 + \ldots, \tag{1.7}$$

where $\Omega \equiv \omega - \omega_l$. The first term correspond to the absolute phase ($E(\Omega)e^{i\phi_l} \rightarrow E(t)e^{i\phi_l}$), the second term to a delay ($E(\Omega)e^{i\omega\phi_1} \rightarrow E(t-\phi_1)$) and the quadratic phase to a linear chirp.

Pulse Duration and Spectral Width of a Gaussian Pulse

There exist several ways to define the duration of a light pulse, or its spectral width. The pulse duration τ_p is most commonly defined as the full width at half the maximum

(FWHM) of the intensity profile $|\mathcal{E}(t)|^2$. The spectral width $\Delta\omega_p$ is then defined as the FWHM of the spectral intensity $|\mathcal{E}(\Omega)|^2$.

For example, an unchirped Gaussian pulse can be described with its temporal amplitude given by:

$$\mathcal{E}(t) = \mathcal{E}_0 \exp\left[-(t/\tau_G)^2\right] \tag{1.8}$$

where the parameter τ_G is used in the calculations instead of τ_p for simplicity. The relation between τ_G and τ_p can be found with the equality $\exp\left[-2(t/\tau_G)^2\right] = 1/2$. We find that $\tau_p = \sqrt{2\ln 2}\ \tau_G$. The corresponding spectral profile $S(\Omega)$ is given by $\exp\left[-\frac{1}{2}\tau_G^2\Omega^2\right]$ and the FWHM, $\Delta\omega_p$, is $4\ln 2/\tau_p$. It follows that the spectral width and pulse duration τ_p are related via the time-bandwidth product:

$$\Delta\omega_p\tau_p = 4\ln 2 \tag{1.9}$$

This corresponds to a Fourier limited pulse since (1.9) is the minimum duration-bandwidth product a pulse can have. For Gaussian pulses, the relation between the pulse duration and spectral width given as a wavelength, derived from (1.9), is given by:

$$\boxed{\Delta\lambda\tau_p = \frac{\lambda^2}{c}\frac{4\ln 2}{2\pi}}, \tag{1.10}$$

where c is the speed of light in vacuum. For example, a Fourier-limited Gaussian pulse, centered at 790 nm with a 9 nm bandwidth will have a duration of 102 fs.

Gaussian Pulse with Linear Frequency Modulation (Chirped)

In the case of a Gaussian pulse with a linear chirp, the electric field in the frequency domain is given by

$$E(\Omega) \propto e^{-\frac{1}{4}\tau_G^2\Omega^2} e^{iA\Omega^2} \tag{1.11}$$

with a chirp parameter A, corresponding to the *quadratic phase term* in (1.7). The intensity profile is the absolute square of the inverse Fourier transform of (1.11)

$$|E(t)|^2 \propto \left| e^{\left(-\frac{t^2\tau_G^2}{16A^2+\tau_G^4}\right)} \exp\left[-i\left(\omega_l t + \frac{4At^2}{16A^2+\tau_G^4}\right)\right]\right|^2 = I(t) \tag{1.12}$$

with a FWHM given by

$$\tau_p' = \sqrt{2\ln 2}\frac{\sqrt{16A^2+\tau_G^4}}{\tau_G}. \tag{1.13}$$

Therefore, for the pulse duration-bandwidth product we find

$$\Delta\omega_p\tau_p' = 4\ln 2\frac{\sqrt{16A^2+\tau_G^4}}{\tau_G^2} = 4\sqrt{2}\ln 2\frac{\sqrt{\tau_p^4+(4A\ln 2)^2}}{\tau_p^2} \tag{1.14}$$

where τ_p' is the new pulse duration after chirping, and τ_p the initial duration of the Fourier-limited pulse. The temporal phase has the general form $\omega_l t+\beta t^2$, with the carrier frequency ω_l, and instantaneous frequency $\omega_l + 2\beta t$. The expression for β as a function of the initial pulse duration and the chirp parameter A is

$$\beta = \frac{4A}{16A^2+\tau_G^4}. \tag{1.15}$$

A Fourier-limited pulse that acquires a quadratic spectral phase will result in a linearly chirped pulse with its spectral amplitude unaffected, but a longer pulse duration. In the limit of large chirp, $\beta \approx \frac{1}{4A}$.

Pulse Propagation and Dispersion

In the previous subsections, we discussed temporal and spectral characteristics of light pulses, neglecting propagation through matter. The general solution of the wave equation in the frequency domain for propagation in the $+z$ direction is [1]

$$E(\omega,z) = |\mathcal{E}(\omega)|e^{-ik(\omega)z}, \tag{1.16}$$

where the propagation constant $k(\omega)$ is determined by the dispersion relation of linear optics

$$k(\omega) = \frac{\omega}{c}n(\omega). \tag{1.17}$$

$n(\omega)$ is the refractive index of the material. We expand $k(\omega)$ about the carrier frequency ω_l

$$k(\omega) = k_l + \delta k, \tag{1.18}$$

where $k_l = \omega_l n(\omega_l)/c$ and

$$\delta k = \left.\frac{dk}{d\omega}\right|_{\omega_l}(\Omega) + \frac{1}{2}\left.\frac{d^2k}{d\omega^2}\right|_{\omega_l}(\Omega)^2 + \ldots. \tag{1.19}$$

The group velocity is defined as $v_g = \left(\frac{dk}{d\omega}\Big|_{\omega_l} \right)^{-1}$, and the second derivative of $k(\omega)$, k_l'', is the group velocity dispersion (GVD). In general, we treat linear pulse propagation through transparent linear media in the frequency domain, since only the phase factor of the field $E(\omega)$ is affected by propagation. The dispersion of a material can be described by either the frequency dependent $n(\omega)$ or the wavelength dependent $n(\lambda)$. The first and second derivative of the wavenumber are given by

$$\frac{dk}{d\omega} = \frac{n}{c} + \frac{\omega}{c}\frac{dn}{d\omega} = \frac{1}{c}\left(n - \lambda \frac{dn}{d\lambda} \right) \tag{1.20}$$

and

$$\frac{d^2k}{d\omega^2} = \frac{2}{c}\frac{dn}{d\omega} + \frac{\omega}{c}\frac{d^2n}{d\omega^2} = \left(\frac{\lambda}{2\pi c} \right) \frac{1}{c}\left(\lambda^2 \frac{d^2n}{d\lambda^2} \right). \tag{1.21}$$

A positive GVD corresponds to $\frac{d^2k}{d\omega^2} > 0$. In the frequency domain, the spectral field after propagation through a thickness z of a linear transparent material is given by:

$$E(\omega, z) = |\mathcal{E}(\omega)| e^{-ik_l z} \exp\left[-izk_l'(\omega - \omega_l) - \frac{izk_l''}{2}(\omega - \omega_l)^2 - \ldots \right] \tag{1.22}$$

where we have expanded the wavevector around an arbitrary frequency ω_l.

1.1.2 Grating-Based Systems for Frequency Modulation

Compressor

Chirping happens "naturally" in any material, because of the dependence of the index of refraction on the wavelengths. The GVD is said to be normal if $\frac{d^2k}{d\omega^2} > 0$ and anomalous when $\frac{d^2k}{d\omega^2} < 0$. In this section, we describe a grating based system that leads to angular dispersion and frequency modulation.

A simple grating configuration is depicted in Figure 1.2 and we refer to the system as the *compressor*[2]. With this optical arrangement, rays of larger wavelength have a larger diffraction angle, and therefore larger delays compared to rays with shorter wavelength at the output of the system. A grating based compressor introduces negative dispersion, and we denote the output pulse as the anti-chirped pulse, or down-chirp pulse. A double pass (not shown) is used to remove the spatial spread of the different frequency components. For chirped-pulse amplification (CPA) [3], this setup is a common choice, since there are

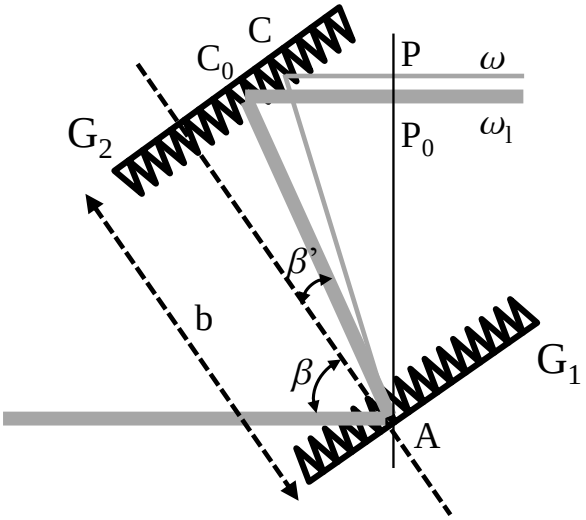

Figure 1.2: Geometrical arrangement of two parallel diffraction gratings used for pulse compression. The system introduces negative group-velocity dispersion and a double pass used to remove the spatial spread of the frequency modes.

no other optical components than the gratings and mirrors that could lead to side-effects such as when the pulses are intense.

Gratings modify the temporal characteristics of short pulses through the difference in the paths taken by different spectral components. Different wavelengths are diffracted by a grating at a different angle. This is called angular dispersion. In figure 1.2 the second grating recollimates the different wavelengths so that at the output of the system there is no net angular dispersion. To determine the dispersion introduced by a pair of parallel gratings, we trace the frequency dependent ray path [2]. The optical path length $\overline{ACP}$ between A and the output virtual line $\overline{PP_0}$ is frequency dependent and, from Figure 1.2, can be determined with help of the figure to be

$$\overline{ACP} = \frac{b}{\cos(\beta')}[1 + \cos(\beta' + \beta)] \tag{1.23}$$

where β is the angle of incidence, β' (< 0) the diffraction angle for the frequency component ω and b is the normal separation between the two gratings. The angles β and β' are related

via the grating equation. For the first order diffraction, the relation is given by [2]

$$\sin(\beta') = \frac{2\pi c}{\omega d} - \sin(\beta), \tag{1.24}$$

where d is the groove spacing. The response of any linear element, including gratings, is of the form [1]

$$R(\omega)e^{-i\Psi(\omega)} \tag{1.25}$$

where we assume that the amplitude $R(\omega)$ is constant over the range of interest and can be neglected. In our apparatus, the phase Ψ is related to the optical path length $\overline{ACP}$ through

$$\Psi(\omega) = \frac{\omega}{c}\overline{ACP}(\omega) + G(\omega). \tag{1.26}$$

The first term corresponds to the phase shift along the path ACP, and $G(\omega)$ is a correction term necessary if taking into account the 2π phase jump at each ruling in first-order diffraction. If was shown in [2] that differentiation of this equation yields the group delay

$$\tau = \frac{d\Psi}{d\omega} = \left(\frac{b}{c}\right)\frac{1+\cos(\beta+\beta')}{\cos(\beta')}. \tag{1.27}$$

Equation (1.27) shows that the group delay is simply equal to the phase delay $\frac{\overline{ACP}}{c}$. The variation of the group delay with frequency can be found by differenting the group delay with respect to ω. If one evaluates the expression at the central frequency ω_l we obtain, in terms of the wavelength [2]:

$$\boxed{\left.\frac{d^2\Psi}{d\omega^2}\right|_{\omega_l} = -\frac{\lambda_l}{2\pi c^2}\left(\frac{\lambda_l}{d}\right)^2 \frac{b}{\cos^3[\beta'(\lambda_l)]}}. \tag{1.28}$$

As an example, consider a grating with 1200 lines/mm, $\lambda_l = 790$nm, and $\beta = 20^o$. For two wavelength components differing by 9 nm, the relative time delay between the two is approximatively 0.43 ps/cm, by separation b.

In [2], we see that a pulse propagating from one grating to the other as shown Figure 1.2 can be considered as having traversed a linear medium of length $L = b/\cos\beta'$ with negative dispersion. The dispersion can be written as:

$$\left.\frac{d^2\Psi}{d\omega^2}\right|_{\omega_l} = k_l'' L = -\left\{\frac{\lambda_l}{2\pi c^2}\left(\frac{\lambda_l}{d}\right)^2 \frac{1}{\cos^2\beta'(\omega)}\right\} L \tag{1.29}$$

Stretcher

We now discuss, in a more illustrative way, a different grating-based configuration presenting positive dispersion, refered to as a *stretcher*. While it is not possible to inverse the sign of the group-velocity dispersion in a compressor without additional optical components, a telescope inserted between two antiparallel gratings modifies the phase shift to invert the sign of the GVD [4]. In Figure 1.3, lenses of the same focal length f are placed at a distance $2f$ from each other and at a distance a from the gratings. The case $a = f$ is used in the pulse shaper [5], in which a spatial light modulator can be employed to generate arbitrary pulse shapes. In this case, the gratings serve only to spatially separate the different frequency components.

When the gratings are situated on both sides of the telescope, at the focal plane of the lenses (O and O'), i.e $a = f$, the optical path between the two focal planes does not depend on the diffraction angle $\beta'(\omega)$. All the rays will travel the same path length, independent of the wavelength, and therefore the net angular dispersion will be zero. A mirror M is used to double-pass the laser beam through the system, both for compactness and to keep all frequencies collinear in a circular beam profile.

For the configuration illustrated in Figure 1.3, the effective length of dispersion is given by [6]

$$l_{eff} = L - 4f \tag{1.30}$$

and is related to the group delay τ

$$\frac{d\tau}{d\omega} \propto -\left[\frac{d\beta'}{d\omega}\right]^2 l_{eff} \tag{1.31}$$

In the configuration used in our experiment, $a < f$, such that l_{eff} is negative, and a positive value for the group-velocity dispersion is expected. By tracing the path length of different frequency components through the setup, one can deduce that the rays with shorter wavelengths ("blue") will experience a larger delay than the rays with longer wavelengths ("red").

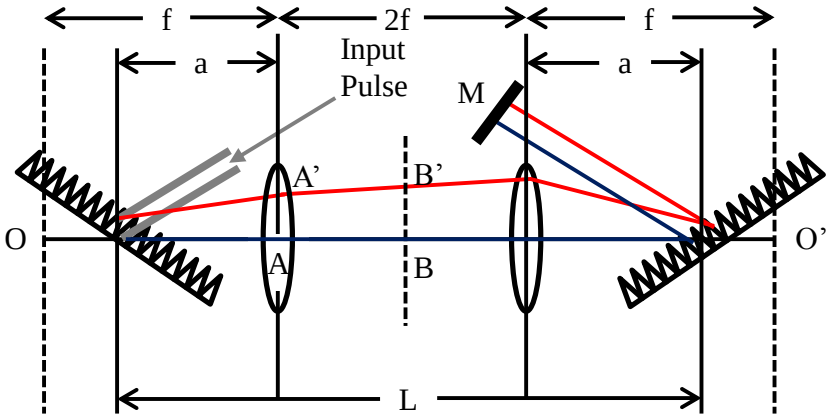

Figure 1.3: Geometrical arrangement of anti-parallel diffraction gratings and a telescope. The system is refered to as a stretcher and introduces positive group-velocity dispersion when $L < 4f$. When the gratings are situated at the focal planes O and O', the path length $\overline{OAB}$ and $\overline{OA'B'}$ are the same for different frequency components and no dispersion is observed.

1.2 Sum Frequency Generation

Sum frequency generation (SFG) is a nonlinear optical phenomenon caused by the nonlinear response of a material to intense optical fields. In order to describe generation of higher harmonics, the polarization of a material can be expressed as a power series in the field strength $E(t)$. Here, we are interested in the second-order nonlinear polarization [7]

$$P^{(2)}(t) = \chi^{(2)} E^2(t), \tag{1.32}$$

where $\chi^{(2)}$ is known as the second-order nonlinear optical susceptibility.

Lets say we have an optical radiation with just two frequency components of the form $E(t) = E_1 e^{-i\omega_1 t} + E_2 e^{-i\omega_2} + c.c$ incident upon a nonlinear crystal with a nonzero nonlinear susceptibility $\chi^{(2)}$ such as in β-BaB2O4 (BBO) crystals. After substitution in (1.32), we see that several terms arise, corresponding to various physical processes. We concentrate on sum-frequency generation (SFG), where $P^{(2)}(t) \sim 2\chi^{(2)} E_1 E_2 e^{-i(\omega_1+\omega_2)t}$ and second-harmonic generation (SHG), where $P^{(2)}(t) \sim \chi^{(2)} E^2_{1(2)} e^{-2i\omega_{1(2)}t}$. SFG is analogous to SHG but more general, since different input frequencies are involved.

As shown in Boyd [7], the intensity of the generated field at frequency $\omega_3 = \omega_1 + \omega_2$ is given by

$$I_3 = I_3(\text{max})\frac{\sin^2(\Delta\text{kL}/2)}{(\Delta\text{kL}/2)^2} \tag{1.33}$$

The SFG is efficient within the spectral bandwidth where the phase mismatch $\Delta kL < \pi$. With this inequality, one can deduce the *acceptance bandwidth* of a given nonlinear crystals [8].

The wavenumber mismatch $\Delta k = k_2 + k_2 - k_3$ is responsible for the decrease in the efficiency of the nonlinear process. For example, when two optical radiations are collinearly incident onto an isotropic optical crystal, normal dispersion does not allow for perfect phase-matching, $\Delta k = 0$, and no field other than the fundamentals will be observed. One way to achieve the phase-matching condition is to make use of the birefringence of a material. In birefringent crystals, the refractive index depends on the direction of the polarization of the electric field. We define the *optic axis* of uniaxial crystals as the axis along which isotropy is broken, and the *optical plane*, as the plane containing the wavevector $\overrightarrow{k}$ and the optic axis. Light polarized perpendicular to the optic plane is called the ordinary "o" polarization and experiences a refractive index n_o. Light polarized parallel to that plane is called the extraordinary polarization "e" and experiences a refractive index $n^e = n^e(\theta)$. The angle θ between the optic axis and $\overrightarrow{k}$ varies when the orientation of the crystal is tuned with respect to the propagation direction of the incident light.

There are two types of phase matching, depending if the fields at frequency ω_1 and ω_2 have the same polarization (Type I) or if they are cross-polarized (Type II). For example, the phase matching condition $\Delta k = 0$ for a negative uniaxial crystal ($n^e < n^o$), using the Type II condition, is given by

$$k_3 = k_1 + k_2 \tag{1.34}$$

$$n_3^e(\theta)\omega_3 = n_1^e(\theta)\omega_1 + n_2^o\omega_2 \tag{1.35}$$

The relation between the extraordinary index of refraction $n^e(\theta)$ and θ is [7]

$$\frac{1}{n_e(\theta)^2} = \frac{\sin^2\theta}{\overline{n_e}^2} + \frac{cos^2\theta}{n_o^2} \tag{1.36}$$

where $\overline{n_e}$ is the principal value of the extraordinary refractive index and can be found in tables [8]. In equation (1.33), the intensity $I_3 = I_3(max)$ when $\Delta k = 0$, and this condition can therefore be satisfied by changing the value of $n_e(\theta)$ by tuning the crystal angle.

1.2.1 Autocorrelator

In this section we are interested in a technique to measure the temporal profile of laser pulses. If the duration of the light pulse is too short to be measured by electronic detectors directly, autocorrelation techniques can be used to measure the temporal width of light pulses emitted from mode-locked lasers. Such a device is called an autocorrelator.

In an autocorrelator, a pulse to be characterized is split into two parts and recombined in a nonlinear crystal after the two parts have experienced a known relative time delay. When the pulses overlap temporally at the crystal the second harmonic intensity signal is measured and the variation of the signal as a function of delay time represents the autocorrelation function of the pulse and is related to the pulse width [1]. In order to estimate the pulse width from the autocorrelation width, a pulse shape has to be assumed. For example, assuming a Gaussian shape, and that the second harmonic field E_{SHG} is proportional to the product of the fundamental fields $E_1(t)$:

$$E_{SHG}(t,\tau) \propto E_1(t)E_1(t-\tau), \tag{1.37}$$

where τ is a variable delay. The spectral intensities are

$$I_{SHG}(t,\tau) \propto |E_1(t)|^2|E_1(t-\tau)|^2 = I_1(t)I_1(t-\tau) \tag{1.38}$$

and the total intensity corresponds to:

$$I_{SHG}(\tau) \propto \int dt I_1(t)I_1(t-\tau). \tag{1.39}$$

Assuming $E_1(t) = E_2(t) = e^{-(\frac{t}{\tau_G})^2}$, the intensity of the autocorrelation becomes $I_{SHG}(\tau) \propto e^{(\frac{\tau}{\tau_G})^2}$ with a FWHM $\tau_P = 2\sqrt{\ln 2}\tau_G$. This is a factor of $\sqrt{2}$ larger than the FWHM of the actual laser pulses with the intensity $I_1 = I_2$.

In figure 1.4, the pulses in different arms of the Michelson interferometer have the same polarization and are combined at a nonlinear crystal phase matched for non-collinear Type I second harmonic generation. In this non-collinear geometry, only the second harmonic light produced is detected. The filter (Fi) is used to block transmission of light at the wavelength of the laser.

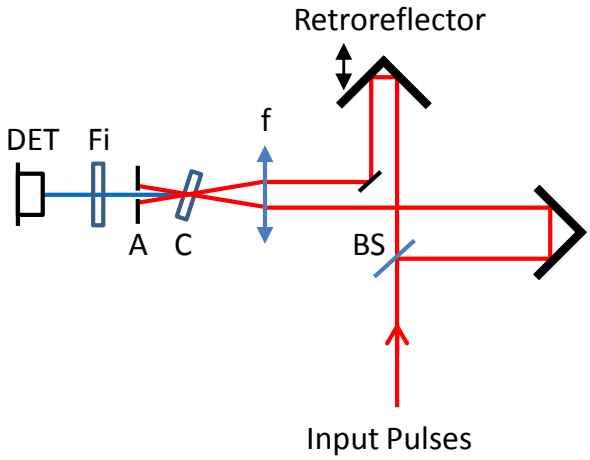

Figure 1.4: .Optical schematic of an autocorrelator for short-pulse duration measurements. The input pulses enter the Michelson interferomter and are split at the 50:50 beam splitter (BS). After retroflection at mirrors in the reference arm and the delayed arm, the beams are focused by a lens (f) onto the thin SHG-crystal (C). The SH field passes through the aperture (A) and a filter (Fi) before detection (DET). The measured intensity in function of the delay gives the autocorrelation, allowing to determine the pulse width.

1.3 White Light Interferometry

In this section, we derive the interferometric signal as measured by a square-law detector at the output of a Mach-Zehnder interferometer with short pulses as the light source. This is an example of white-light, or short-pulse interferometry. We will also discuss the origin of signal deterioration when dispersive material is inserted in one of the arms.

Let us consider the basic Mach-Zehnder interferometer sketched in Figure 1.5. We assume perfect beam splitters and identical mirrors in both paths. Without dispersive material inserted, the field at the output beam splitter (BS2) is given by:

$$E(t, \Delta\tau) = E_1(t - \Delta\tau) + E_2(t). \tag{1.40}$$

$\Delta\tau$ is the delay parameter, and allows to vary the phase between the two amplitudes. The intensity at the output of the interferometer is proportional to the electric field squared, averaged over the detector's response time, on the order of $10^{-13} - 10^{-12}$ s.

We describe the input field with a real spectral amplitude, centered around the average frequency of the radiation ω_l, given by $\mathcal{E}(\Omega) = e^{-\frac{(\omega-\omega_l)^2}{2\sigma^2}} = e^{-\frac{\Omega^2}{2\sigma^2}}$. Here, σ is the standard deviation and is directly related to the FWHM of the spectral intensity: $\sigma_p = 2\sqrt{\ln 2}\sigma$. At the output beam splitter, the electric field for one frequency component is

$$E(\Omega, \Delta\tau) = e^{-\frac{\Omega^2}{2\sigma^2}} \left(1 + \exp[-i(\omega_l + \Omega)\Delta\tau]\right) \tag{1.41}$$

The actual signal recorded at the output of the interferometer by a square-law detector is the intensity $I(\Delta\tau)$ given by

$$I(\Delta\tau) = \int d\Omega |E(\Omega)|^2 \tag{1.42}$$

and becomes, after normalization:

$$\boxed{I(\Delta\tau) = \frac{1}{2} + \frac{1}{2} e^{-\frac{1}{4}\Delta\tau^2\sigma^2} \cos\left[(\Delta\tau)\omega_l\right]}. \tag{1.43}$$

Because of the short coherence length of the radiation ($\frac{4\sqrt{\ln 2}}{\sigma}$), the delay range over which a fringe pattern can be observed is restricted. For example, a Fourier-limited Gaussian pulse with a bandwidth of 9nm centered at 790nm will be "coherent" with itself over a 204 fs delay, or 61 μm. Note that it is twice the pulse duration.

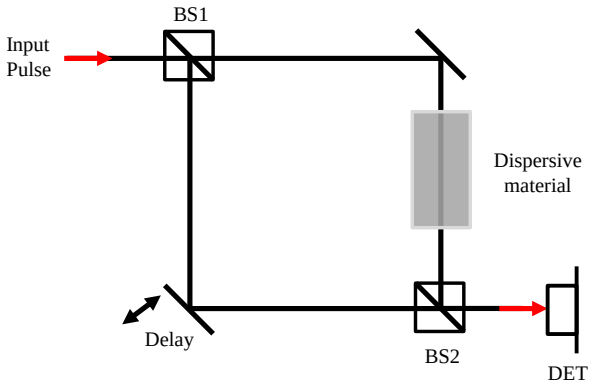

Figure 1.5: White-Light Mach-Zehnder interferometer.

We now consider a transparent material characterized by a transfer function $H(\Omega)$ inserted in the "sample" arm. After the output beam splitter, the total electric field for one frequency component is given by

$$E(\Omega, \Delta\tau) = \sqrt{S(\Omega)}\left[H(\omega_l + \Omega) + \exp[-i(\omega_l + \Omega)\Delta\tau]\right] \tag{1.44}$$

where $S(\Omega)$ is the spectral intensity $\propto e^{-\frac{\Omega^2}{\sigma^2}}$. Following the derivation in [9], the interferogram, $I(\Delta\tau)$, measured corresponds to

$$\begin{aligned} I(\Delta\tau) &= \int d\Omega \left[1 + |H(\omega_l + \Omega)|^2\right] S(\Omega) \\ &+ 2\mathrm{Re}\left\{\int d\Omega H(\omega_l + \Omega) S(\Omega) e^{-i\Omega\Delta\tau} e^{-i\omega_l\Delta\tau}\right\} \end{aligned} \tag{1.45}$$

For simplicity, let's consider the case $H(\Omega) = e^{ik(\Omega)L}$, with the wavenumber $k(\Omega)$ as defined in (1.17), and L corresponding to the length of the transparent medium. $k(\Omega)$ is expanded up to second order as in (1.18) and (1.19). If we first neglect the GVD (k''), the envelope of the interferogram becomes delayed by $k'L = L/v_g$ compared to the signal without the dispersive medium present, where v_g is the group velocity of the wave envelope. We note that the introduction of a dispersive medium leads to a shift of the center of the interference pattern. This is due to the longer time needed for light to traverse the sample instead of air.

The GVD causes different parts of the pulse spectrum to travel at different velocities, resulting in pulse deformation and chirping. To illustrate this idea, we derive the new

FWHM of the interferometric signal as measured at the output of the interferometer. We use the last term of Equation (1.45), and assume second-order dispersion, such that $H(\Omega) = e^{-i\beta\Omega^2}$ and a spectral intensity $S(\Omega) = e^{-\Omega^2/\sigma^2}$, with σ as the RMS spectral width. The dispersive term, β, correspond to $\frac{1}{2}k_l''L$ evaluated at a central frequency ω_l. The amplitude of the interference pattern is given by

$$\exp\left[-\frac{1}{4}\frac{\Delta\tau^2\sigma^2}{(1+\beta^2\sigma^4)}\right] \tag{1.46}$$

and its FWHM will correspond to

$$\tau_{FWHM}(\beta) = 4\sqrt{\ln 2}\frac{\sqrt{1+\beta^2\sigma^4}}{\sigma}. \tag{1.47}$$

The width of the interference pattern is clearly broadened by the dispersive term β. This distortion can be important and makes the measured interferogram unreliable.

Interference of short laser pulses is widely used in optical coherence tomography (OCT) [10]. Typically, light is *reflected* from the interfaces between different layers of a sample placed in one of the arms, and interferes with a reference beam delayed with respect to the former. The mathematical formalism is identical to the one used for a transparent medium, but using a sample model represented by a discrete summation of the form [9]

$$H(\Omega) = \sum_j r_j(\Omega)e^{i2\Psi_j(\Omega)}, \tag{1.48}$$

where the index j corresponds to different layers that constitute the sample. Interference fringes will appear when the relative path delay is within the coherence length of the light source. The resolution achievable with this technique is directly related to the bandwidth of the light ($\sim 1/\sigma$) but as we have shown, the interferogram will be increasingly distorted and broadened by GVD.

1.4 Two-Photon Quantum Interference

Two-photon quantum interference was first observed in 1987 by Hong, Ou, and Mandel [11]. Two identical photons were sent simultaneously through the different input modes, a and b, of a 50:50 beam splitter as depicted in Figure 1.6. With a photon detector in each of the output modes c and d, no coincidence detections occured.

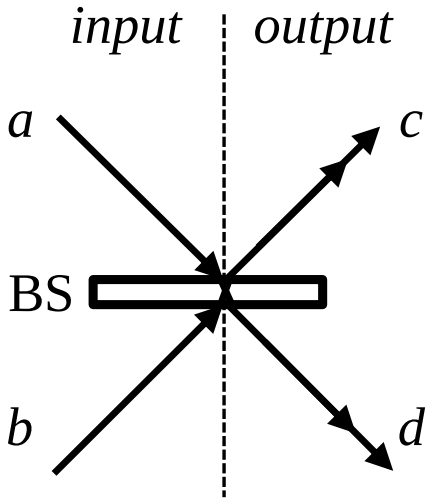

Figure 1.6: Two photons incident in different input modes of a 50:50 beam splitter.

In the preceding section, we described a classical interference effect that was shown to give information about the coherence time of a light pulse, and how this effect could be used to characterize samples. Here we discuss fourth-order interference, i.e. an interferometric effect in which the interference occurs in coincidences between two detectors. It will be shown that this effect contains advantages over the scheme using white-light, especially when a highly dispersive material is involved.

We first consider two identical photons entering the different input ports of a 50:50 beam splitter as depicted in Figure 1.6. The input state is given by $|\Phi_{in}\rangle = a^\dagger b^\dagger |0\rangle$, where $a^\dagger(b^\dagger)$ is the creation operator in mode $a(b)$ and $|0\rangle$ is the vacuum state when no particles are found in the input modes. The beam splitter will prepare the system in the state

$$\begin{aligned} |\Phi_{out}\rangle &= \frac{1}{2}\left(c^\dagger + d^\dagger\right)\left(c^\dagger - d^\dagger\right)|0\rangle \\ &= \frac{1}{2}\left[\left(c^\dagger\right)^2 - c^\dagger d^\dagger + d^\dagger c^\dagger - \left(d^\dagger\right)^2\right]|0\rangle. \end{aligned} \tag{1.49}$$

Since photons are bosons, they obey the commutation relations [12]

$$[c^\dagger, d^\dagger] = c^\dagger d^\dagger - c^\dagger d^\dagger = 0 \tag{1.50}$$

We are left with the output state

$$|\Phi_{out}\rangle = \frac{1}{2}\left[(c^\dagger)^2 - (d^\dagger)^2\right], \tag{1.51}$$

which implies a zero coincidence count rate at the output ports.

1.4.1 Dispersion Cancellation

In a follow-up experiment to the original HOM interference experiment, it has been shown that all even-order dispersions have no net effect on the final interferogram, when a dispersive medium is inserted in one arm of the HOM interferometer [12]. Here, we briefly explain how the time interval between photons emitted in spontaneous parametric down-conversion can be used to measure the coherence length of the two-photon wave packet. Furthermore, since the technique is insensitive to even orders of GVD, one can accurately measure the group delay experienced by the photons inside a dispersive material.

We first consider the HOM interferometer, without dispersive element, as depicted in Figure 1.7. Two photons are simultaneously generated via spontaneous parametric down-conversion in a crystal with a $\chi^{(2)}$ nonlinearity. Let the frequencies of the two photons be ω_1 and ω_2, respectively. Because of energy conservation, the relation $\omega_1 + \omega_2 = \omega_{pump}$ must hold, where ω_{pump} is the center frequency of the narrow-bandwidth pump beam. The emitted photons are brought together on a 50:50 beam splitter (BS). The rate of coincidences, within a short coincidence time window, is measured for different relative time delays between the photons at the BS. The coincidence count rate vanishes as the path-length difference goes to zero, as described in the previous section.

A simplified explanation of the HOM effect is that interference occurs only when the two photons overlap at the beam splitter. As the time delay between the photons at the BS increases, they become more and more distinguishable, until they become fully discernable when the delay exceed their coherence length. The interference pattern has the shape of a "dip"in the coincidence rate vs delay.

When dispersion comes into play, the interpretation needs to be modified. In Figure 1.7, one of the down-converted photons passes through the dispersive material in the spatial mode a while the conjugated photon acquires a variable delay in mode b. The photon which has traveled through the dispersive medium will exhibit a frequency chirp. Specifically, here we assume a material with normal dispersion, such that at the glass output, the "blue" part of the photon wave packet lags behind the the "red" part. One could expect a deterioration of the interferogram due to dispersion. However, no such deterioration occurs

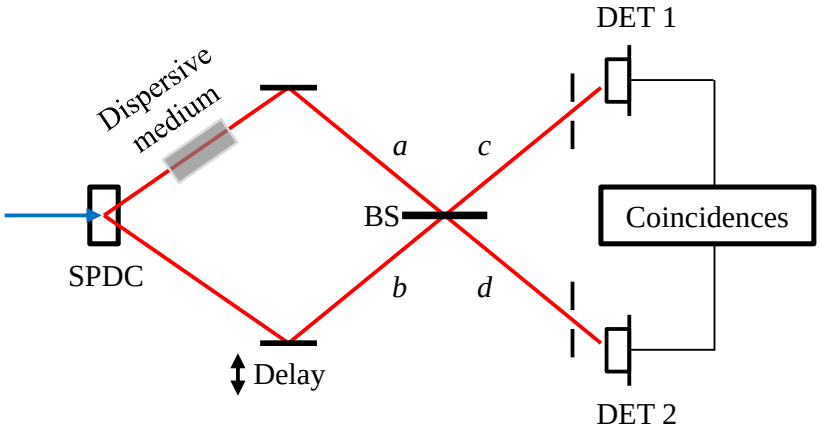

Figure 1.7: Hong-Ou-Mandel (HOM) interferometer with a dispersive medium inserted. A pair of frequency-entangled photons is generated in a nonlinear crystal pumped by a narrow-band pump beam via spontaneous parametric down-conversion. The two-photon state evolves through the interferometer, and the coincidence rate is recorded after the beam splitter (BS) as the delay in one of the arms is scanned.

if we consider up to second-order dispersion, and all other even orders of dispersion, in the wavenumber expansion.

The interference takes place between the two "paths" whose coincidence detection events differ in no observable way. They are often called Feynman paths and lead to indistinguishable outcomes. In the HOM interferometer, the two paths are as follows: Both photons are transmitted at the beam splitter ($a \searrow d$ & $b \nearrow c$) or both photons are reflected ($a \searrow\nearrow c$ & $b \nearrow\searrow d$). For those two paths to be indistinguishable, the center of each photon wave packet must overlap at the BS, and the frequency of the photon registered at a given detector must be the same in both interfering paths. As an example, consider the first path where detector 2 (DET 2) is excited a little bit earlier than the center of the wave packet, by a "redder" component of the frequency-chirped wave packet, when the detector 1 (DET 1) absorbed the "blue" part of the conjugated photon. In the second path, DET 1 is excited a little bit later than the center, by a "bluer" component of the frequency-chirped wave packet, while DET 2 register the "red" part of the conjugated photon. In both cases, the time lag is exactly the same and it cannot be known, even in

principle, which of the two photons traveled through the glass. In other words, these two final states are equivalent and can interfere.

There is a more rigorous explanation of dispersion cancellation, and this is the central result in [12]. The expression of the final coincidence rate in function of the path delay is given by:

$$C(\Delta\tau) \propto \int d\Omega |f(\Omega)|^2 \{1 - \cos[2\Omega(\Delta\tau - \alpha d)]\} \tag{1.52}$$

where $\Omega = \omega_1 - \omega_0 = \omega_0 - \omega_2$ and ω_0 is half the pump frequency. $f(\Omega)$ is the bandwidth function describing the spectrum of the down-converted light and $\alpha = 1/v_g$. The interference term described by this expression depends only on the phase difference between the amplitude of the two-photon state, for the two indistinguishable paths leading to a coincidence event [12]. Since the frequencies of the down-converted photons are assumed to be anti-correlated and symmetric around the central frequency ω_0 this leads to the same phase from the $\beta(\pm\Omega)^2$ term responsible for dispersive broadening. We also have the same effect for higher even-orders. Therefore, in the final coincidence rate (1.52) the term responsible for GVD, β, does not appear. In other words, despite the dispersive broadening in the sample arm, it will have no repercussion on the final forth-order interference pattern. However, the "dip" will be shifted by the same amount as in the white-light interferometer, i.e. $\Delta\tau = L/v_g$ where L is the thickness of the dispersive medium. The signal has 100% visibility and a width determined by the bandwidth function describing the spectrum of the down-converted light at the detectors.

1.4.2 Application to Optical Coherence Tomography

We have seen that the fourth-order interference measured in the HOM interferometer was immune against first-order group-velocity dispersion. A direct application is to use this advantage in optical-coherence tomography. Quantum-optical coherence tomography has been demonstrated [13] by carrying out tomographic measurements with dispersion-canceled resolution. Here we describe the basic principles.

The setup for quantum-optical coherence tomography (QOCT) is depicted in Figure 1.8. The photon pairs evolve the same way through the interferometer as in Figure 1.7 but instead of having a block of dispersive material in one of the arms, a sample allowing multiple reflections is used. For the purpose of calculations, the sample investigated is

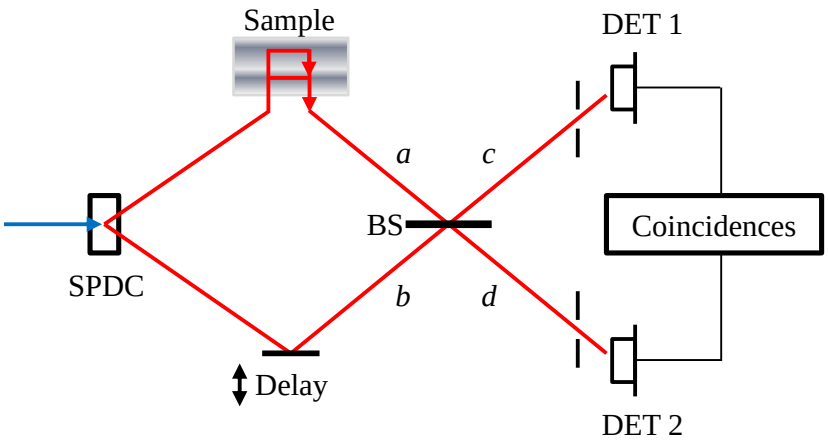

Figure 1.8: Schematic of the HOM interferometer for quantum-optical coherence tomography. Two frequency-entangled photons are simultaneously generated in a nonlinear crystal via spontaneous parametric down-conversion. A sample is inserted in one of the arms and the coincidence rate is recorded after the beam splitter (BS) as the delay in one of the arms is scanned. A dip is observed for each zero delay between a photon traveling in the reference arm and its conjugate photon reflected from one of the sample layers.

idealized by representing it with the same transfer function $H(\Omega)$ as in (1.48). For example, a thin glass plate will have a transfer function given by

$$H(\Omega) = r_1 + r_2 e^{i2k(\Omega)L} \tag{1.53}$$

where r_1 and r_2 are the reflection amplitudes from the front and the back surfaces at normal incidence, L is the sample thickness and c the speed of light in vacuum.

The two-photon state emitted by down-conversion can, to good approximation, be written as [12]

$$|\Psi\rangle = \int d\Omega f(\Omega)|\omega_l + \Omega, \omega_l - \Omega\rangle \tag{1.54}$$

with Ω as the angular frequency deviation about the central frequency $\omega_{pump}/2$ and $f(\Omega)$ as the spectral amplitude of the two-photon wave packet. The spectral distribution is given by $S(\Omega) = |f(\Omega)|^2$. The coincidence rate $C(\Delta\tau)$ will correspond to

$$C(\Delta\tau) \propto \int d\Omega |H(\Omega)|^2 S(\Omega) - \mathrm{Re}\left\{ \int d\Omega H(\Omega) H^*(-\Omega) S(\Omega) e^{-2i\Omega\Delta\tau} \right\}. \tag{1.55}$$

$H^*(\Omega)$ is the complex conjugate of $H(\Omega)$. Dispersion cancellation will occur for all even orders in the expansion of $k(\omega)$.

QOCT yields some advantages over classical OCT. There is a factor of 2 enhancement in the resolution for the same source bandwidth, and the sample group-velocity dispersion does not lead to deterioration of the resolution, at least in leading order. However, up to now, available sources of entangled-photon pairs are weak and QOCT requires long integration times for reliable detection and reasonable signal-to-noise ratios [9].

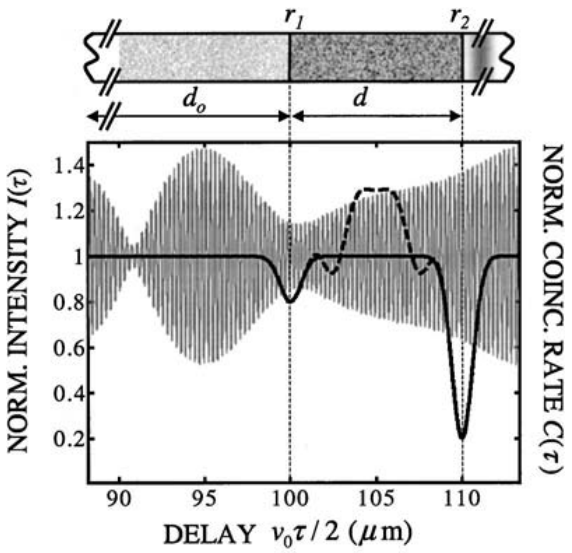

Figure 1.9: Numerical simulation of quantum-OCT and OCT scans demonstrating dispersion cancellation (from Abouraddy et al. [9]). The thin rapidly varying curve corresponds to the normalized intensity $I(\tau)$ of the OCT interferogram and the thick black curves to the normalized coincidence rate $C(\tau)$ of QOCT. The structure of the two-layer sample buried under a dispersive medium is shown at the top of the figure. The OCT signal yields no useful information about the sample structure, whereas the QOCT signal clearly reveals the surfaces in the sample.

Chapter 2

Chirped-Pulse Interferometry

2.1 Motivation

Coherence of light and the effect of interference are perfect means when accurate length measurements have to be determined on a submicron scale. In order to achieve absolute position measurements, a light source with a short coherence length (large bandwidth) is best [10]. However, as the spectral width of the light source increases, negative effects due to dispersion emerge and degrade the quality of the interferograms.

The goal of this chapter is to introduce Chirped-Pulse Interferometry (CPI). This is a new approach, designed to produce the same features as the HOM interferometer [11] *without* the need for quantum resources. Quantum resources are hard to make and very fragile, thus our method has significant practical advantages.

2.2 Theoretical Background of CPI

We have reviewed the properties of nonlinear mixing (SHG & SFG) in section 1.2 and showed that the nonlinear polarization $P_{NL}^{(2)}$ and the second harmonic field generated from an up-converting crystal is proportional to the input field squared (Equation 1.32). In this section, we derive the CPI signal observed at the output of a two-path interferometer, using oppositely chirped laser pulses as the input light source. Assuming narrow-band filtering, the signal of interest consists of two cross-correlation terms generated at a nonlinear

crystal and their destructive interference when the path lengths between the two arms are balanced.

Two different approaches are possible when deriving the CPI interferogram expected at the output detector. The simplified calculations assume infinitely chirped pulses, such that we can consider monochromatic waves propagating through the interferometer and the output signal is given by the summed intensities of all frequency-pair contributions. The second approach is experimentally accessible in the sense that a finite chirp rate is considered. However, we show that in the case where the strength of the quadratic phase induced by a dispersive material is small compared to the strength of quadratic phase inherent to the chirped pulses, the infinite-chirp limit is a very good approximation.

2.2.1 Dispersion Cancellation in the Infinite-Chirp Limit

We first consider the limit of infinite chirp. A simplified version of our interferometer is depicted in Fig 2.1. The "infinitely" chirped pulses are coincident at the input beam splitter (BS), and at any given time, we assume that they have anti-correlated frequencies $\omega_1 = \omega_l - \Omega$ and $\omega_2 = \omega_l + \Omega$. When the lengths of the two interferometric arms are matched, the sum-frequency generated in the nonlinear crystal will be:

$$\omega_1 + \omega_2 = 2\omega_l \tag{2.1}$$

where ω_l is the center frequency of the laser pulses.

The light evolves through the interferometer in such a way that at the output of the nonlinear crystal, two different physical processes are equally probable. The first one, of lower interest, is the autocorrelations of identical frequency components through second-harmonic generation (SHG). The autocorrelation of the down-chirp adds up with the autocorrelation of the up-chirp to produce the total electric field E^A equal to

$$E^A \propto E(\omega_1, \phi(\omega))E(\omega_1, \Delta\tau) + E(\omega_2, \phi(\omega))E(\omega_2, \Delta\tau) \tag{2.2}$$

where $\phi(\omega)$ and $\Delta\tau$ represent the phase and delay picked up in the sample arm and reference arm, respectively. The frequencies of the two auto-correlation terms correspond to $2\omega_1 = 2\omega_l - 2\Omega$ and $2\omega_2 = 2\omega_l + 2\Omega$. After integration over all Ω, this process will lead to a broad spectral background with a negligible contribution to the final signal after

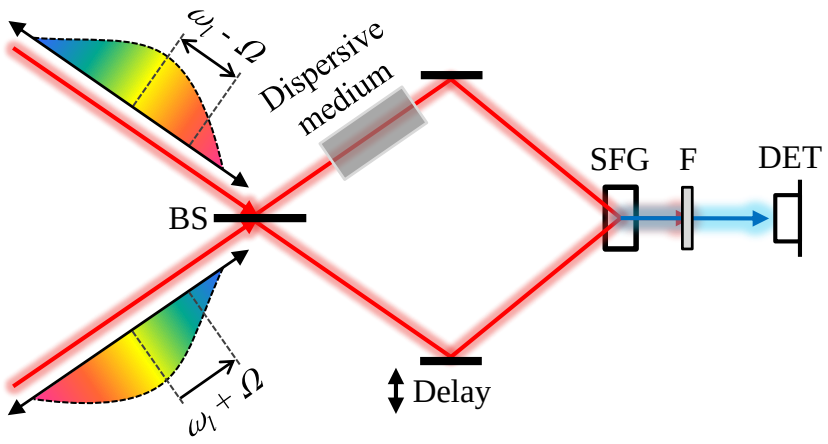

Figure 2.1: Schematic of the chirped-pulse cross-correlator. In the infinite-chirp limit, at any given time, the two beams entering the interferometer have anti-correlated frequencies $\omega_l - \Omega$ and $\omega_l + \Omega$. The beam splitter (BS) will create a superposition of an up-chirp and down-chirp in the sample arm and in the delay arm. After the two beams undergo sum-frequency generation (SFG) at the nonlinear crystal, spectral filtering (F) allows detection of the cross-correlation terms from anti-correlated frequencies only, in a spectral window centered at $2\omega_l$.

spectral filtering. For simplicity, we will neglect the auto-correlation contributions in the system, without affecting the main results.

The second process, at the heart of CPI, is the cross-correlation from anti-correlated frequency components through sum-frequency generation (SFG). In the sample arm, the electric field will acquire a spectral phase from the dispersive material modeled by $H(\omega)$. Electric fields in the reference arm will encounter a delay resulting in a phase term $e^{i\omega\Delta\tau}$.

The electric field of the frequency component $\omega_1 = \omega_l - \Omega$ can either be reflected at the beam splitter ($\rightarrow H(\omega_1)E_1$), or be transmitted in the delay arm $\left(\rightarrow E_1 e^{i\omega_1\Delta\tau}\right)$. The electric field of the frequency component $\omega_2 = \omega_l + \Omega$ can also be transmitted through the BS ($\rightarrow H(\omega_2)E_2$) or be reflected $\left(\rightarrow -E_2 e^{i\omega_2\Delta\tau}\right)$, and acquires a minus sign due to the BS. The SFG field E^{SFG} generated in the nonlinear crystal is

$$\begin{aligned} E^{SFG} &\propto \left[\sqrt{S(\Omega)}e^{i(\omega_l-\Omega)t}e^{i(\omega_l-\Omega)\Delta\tau}\right]\left[\sqrt{S(\Omega)}H(\omega_2)e^{i(\omega_l+\Omega)t}\right] \\ &- \left[\sqrt{S(\Omega)}e^{i(\omega_l+\Omega)t}e^{i(\omega_l+\Omega)\Delta\tau}\right]\left[\sqrt{S(\Omega)}H(\omega_1)e^{i(\omega_l-\Omega)t}\right] \end{aligned} \tag{2.3}$$

where we assumed that the two pulses have the same Gaussian spectral intensity $S(\Omega)$. To find the final intensity $C(\Delta\tau)$ measured at the output of the interferometer, we take the modulus square of E^C and integrate over all the frequencies contained in the distribution $S(\Omega)$. The expression, becomes

$$C(\Delta\tau) = \int d\Omega \left[S(\Omega)\right]^2 \left[|H(\omega_2)|^2 + |H(\omega_1)|^2\right] \tag{2.4}$$

$$-2\mathrm{Re}\int d\Omega \left[S(\Omega)\right]^2 H(\omega_1)H^*(\omega_2)e^{-i2\Omega\Delta\tau} \tag{2.5}$$

Let us consider a block of dispersive material as the sample, such that

$$H(\omega) = e^{-ik(\omega)L}. \tag{2.6}$$

We expand $k(\omega)$ around the center frequency ω_l

$$k(\omega_1) = k_l + \alpha(-\Omega) + \beta(-\Omega)^2 + \ldots \tag{2.7}$$

$$k(\omega_2) = k_l + \alpha(+\Omega) + \beta(+\Omega)^2 + \ldots \tag{2.8}$$

where $\alpha = \frac{dk}{d\omega}|_{\omega_l}$ is the inverse of the group delay and $\beta = \frac{1}{2}\frac{d^2k}{d\omega^2}|_{\omega_l}$ defines the second order group velocity dispersion (GVD). Using equations (2.6-2.8), we have $|H(\omega)|^2 = 1$ and

$$\begin{aligned} H(\omega_1)H^*(\omega_2) &= e^{i(k(\omega_2)-k(\omega_1))L} \\ &\cong e^{i\alpha 2\Omega L} \end{aligned} \tag{2.9}$$

For the last expression, we have used equations (2.7&2.8) and only included terms up to second order in Ω. We see that the second-order term vanishes, and the same holds for all even-order terms. With dispersion in one arm, the measured signal is therefore given by:

$$C(\Delta\tau) \propto \int d\Omega \ [S(\Omega)]^2 - \int d\Omega \, [S(\Omega)]^2 \cos\left[2\Omega(\alpha L - \Delta\tau)\right] \tag{2.10}$$

After normalization, we have

$$C(\Delta\tau) = 1 - \frac{\int d\Omega \ [S(\Omega)]^2 \cos\left[2\Omega(\alpha L - \Delta\tau)\right]}{\int d\Omega \ [S(\Omega)]^2} \tag{2.11}$$

In the previous expression, when $\alpha L - \Delta\tau = 0$, the extra time of flight of light traversing the sample arm is compensated by the delay in the reference arm. To find an analytical expression for the integrals we assume a Gaussian spectral shape with $S(\Omega) = e^{-\frac{\Omega^2}{\sigma^2}}$, where σ is the RMS bandwidth of the electric field. The normalized signal becomes

$$C(\Delta\tau) = 1 - e^{-\frac{1}{2}\sigma^2(\alpha L - \Delta\tau)^2} \tag{2.12}$$

The normalized CPI interferogram is sketched in Figure 2.2. The full-width at half the maximum is

$$\Delta\tau_{FWHM} = \frac{2\sqrt{2\ln 2}}{\sigma} \tag{2.13}$$

From this expression, one can define the resolution of the measurement Δl as the FWHM of the dip, and using wavelengths instead of frequencies,

$$\Delta l = \frac{2\sqrt{2}\ln 2}{\pi} \frac{\lambda_0^2}{\Delta\lambda} \tag{2.14}$$

where λ_0 is the center wavelength.

Let us highlight the features of CPI interferograms. Firstly, the resolution given by (2.14) has no dependence on the second-order group-velocity dispersion β, responsible for distortion in white-light interferograms. Since the output signal depends only on the phase difference between the two cross-correlation terms in (2.3), assuming perfect anti-correlation between oppositely-chirped pulses implies that $(\omega_1 - \omega_l)^2 = (\omega_2 - \omega_l)^2$, therefore the dispersion term vanishes in (2.9). Secondly, comparing the coherence length given by Equation (2.14) and the coherence length of a white-light interferogram, CPI demonstrates an inherent $\sqrt{2}$ resolution improvement over white-light interferometry, for Gaussian pulse

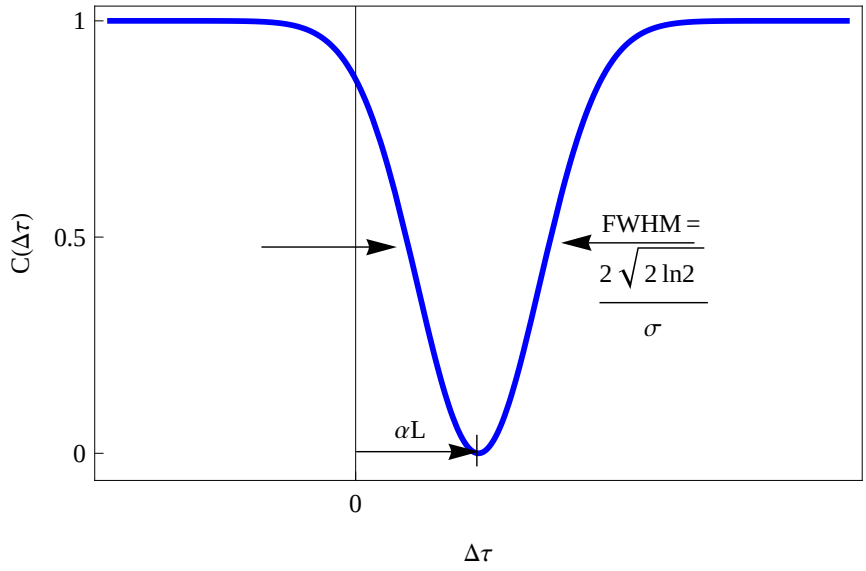

Figure 2.2: CPI interference dip (Theory). For relative delays ($\Delta\tau$) longer than the coherence length (FWHM) of the input light the signal is constant. The signal demonstrates perfect contrast when the delay becomes null, given that the auto-correlation background is neglected. The absolute position of the zero-delay will depend on the amount of dispersive material inserted in one arm.

shapes. Thirdly, the CPI signal demonstrates a perfect visibility phase insensitive dip, in the sense that no interference fringes are observed. Finally, it will be shown experimentally that the dip visibility is also insensitive to unbalanced loss between the interferometric arms.

2.2.2 Dispersion Cancellation with Realistic (Finite) Chirp

In the previous section, we have considered CPI calculations in the unphysical approximation of infinite chirp. In this limit, at any given time inside the interferometer we have two monochromatic waves of anti-correlated frequencies. The fields were approximated with δ-functions in the frequency domain. In general, the nonlinear polarization (here the second order only) in the frequency domain is a convolution [1]:

$$P^{(2)}(\omega) = \int P^{(2)}(t)e^{-i\omega t}dt = \epsilon_0\chi_0^{(2)} \int E_1(\omega-\omega')E_2(\omega')d\omega' \tag{2.15}$$

where an instantaneous nonlinearity is assumed, such that $\chi^{(2)}$ is a constant over the frequency range of interest. Equation (2.15) reflects the fact that many frequency pairs can be phase matched to sum up to the polarization at a given frequency, and all add coherently. Like we did in [14], we make the approximation that the radiated field from the nonlinear crystal is proportional to the polarization. The SFG electric field amplitude in the frequency domain becomes

$$E_{SFG}(\omega) \propto \int d\omega' E_1(\omega')E_2(\omega-\omega'). \tag{2.16}$$

We write the electric field amplitudes for the linearly chirped pulses as

$$E(\omega; A) = E_0 e^{\frac{(\omega-\omega_l)^2}{2\sigma^2}} e^{iA(\omega-\omega_l)^2} \tag{2.17}$$

where σ is the RMS bandwidth of the field and A is the chirp parameter which can be positive or negative. The oppositely chirped pulses are overlapped at the input beam splitter of the interferometer, as shown in Figure 2.1. The field in the delay arm is written as:

$$E_1(\omega, \Delta\tau) = \left[E(\omega; A) + E(\omega; -A)\right] e^{i\omega\Delta\tau}. \tag{2.18}$$

In the sample arm, we assume the presence of transparent material with purely quadratic dispersion ($\phi(\omega) = \epsilon(\omega-\omega_l)^2$), i.e. we ignore the group delay which leads to an offset

of the interference from $\Delta\tau = 0$ (see previous section). After the dispersive sample, the electric field is written as:

$$E_2(\omega) = [E(\omega; A) - E(\omega; -A)]\, e^{i\epsilon(\omega-\omega_l)^2}, \tag{2.19}$$

where the minus sign reflects the π phase shift acquired at the input beam splitter.

For the following calculations, we make the assumption that the laser pulses have large chirp, such that the pulse durations are much longer than the Fourier-limited pulse duration. In that limit, the SFG from the cross-correlations will have a much narrower bandwidth than the auto-correlations such that we can ignore the contribution from the auto-correlations. The expression for the electric field of the cross-correlations is given by

$$E_{SFG}(\omega, \Delta\tau) \approx \int d\omega' \left[E(\omega'; -A)E(\omega - \omega'; A) - E(\omega'; A)E(\omega - \omega'; -A)\right] e^{i\Delta\tau\omega'} e^{i\epsilon(\omega-\omega'-\omega_l)^2}. \tag{2.20}$$

CPI signal is then given by [14]:

$$I_{CPI}(\Delta\tau) \propto \int d\omega |E_{SFG}(\omega, \Delta\tau)|^2 \tag{2.21}$$

The results show that when the chirp parameter A is large compared to the dispersion ϵ the visibility of the CPI dip is maximal, while deviation from this limit affects the visibility. One can also derive that the broadening of the dip width is proportional to $\epsilon\frac{\tau_\epsilon}{\tau_{chirp}}$, where τ_ϵ is the time duration of a Fourier-limited pulse subjected to the dispersive phase $\phi(\omega)$ and τ_{chirp} is the time duration of the chirped pulse. Thus, as the chirp pulse duration goes to infinity, the dispersion cancellation becomes perfect. Also, this tells us that the chirp rate must be large compared with the dispersion.

2.3 Experimental Demonstration of Chirped-Pulse Interferometry

2.3.1 Experimental Setup and Methods

To demonstrate the principles of CPI, we use a configuration as depicted in Figure 2.3. The source of light is a pulsed Ti-sapphire oscillator with an average power of 2.8 W, a

center wavelength of 790 nm, pulse width of 110 fs FWHM and repetition rate of 80 MHz. The polarization, originally vertical, is rotated to horizontal, i.e. parallel to the optical table, for optimal diffraction efficiency from our gratings. The pulses are split on a 50/50 beam splitter. One half passes through a grating-based optical compressor and the other half through stretcher, as described in Section 1.1. Because the original pulses are Fourier-limited, both, compressor and stretcher, increase the pulse duration of the initial pulses but with opposite group-velocity dispersion. Our ruled diffraction gratings are 30 mm x 30 mm, 1200 lines mm^{-1} gold-coated, blazed for 800 nm.

The normal distance between the compressor's two gratings is 56 cm, and the incident angle is about 20^o. The spectral width at the output of the system is 9 nm, and using Equation (1.28), we expect a pulse duration of 46.4 ps. The pulse duration of the 790 mW down-chirped pulse using the CPI cross-correlator was measured to be 45.1 ± 0.1 ps.

The separation between the gratings in the stretcher is 145 cm. The telescope is built using two lenses of ~ 50 cm focal length so that the effective length in Equation (1.30) is -55 cm. The output up-chirped pulses are measured to be 51.2 ± 0.2 ps long with 10 nm bandwidth and average power of 870 mW. It is close to the expected 52.5 ps duration. The difference between the duration of the up- and down-chirped pulses is due to unequal loss of spectral components in the compressor and stretcher.

The beams from the compressor and stretcher are spatially and temporally overlapped at the input beam splitter cube of the cross-correlator shown in Figure 2.3. The length of the path taken by down-chirped pulses from the compressor to the BS can be varied by translating a retroreflector. The oppositely chirped pulses are centered at 790 nm, and we set the delay (ΔT) such that at the output of the cross-correlator input BS, the spectral intensity exhibits a narrow-band interference at the central frequency $\sim \omega_l$. This spatial overlap will have a direct impact on the final center SHG wavelength. This wavelength will be equal to $2\omega_l$ for perfect overlap, or $2\omega_l + 2\delta\omega(\Delta T)$, depending on the delay ΔT between the up-chirp and down-chirp at the BS.

The two outputs of the beam splitter lead to different arms of the cross-correlator. One is called the delay arm, where a retroreflector is placed on a motorized translation stage with 40 mm travel range. The other is the sample arm, with a dispersive material, characterized by the transfer function $H(\Omega)$, inserted before a half-wave plate (HWP), which rotates the polarization from horizontal to vertical. Light evolving through these

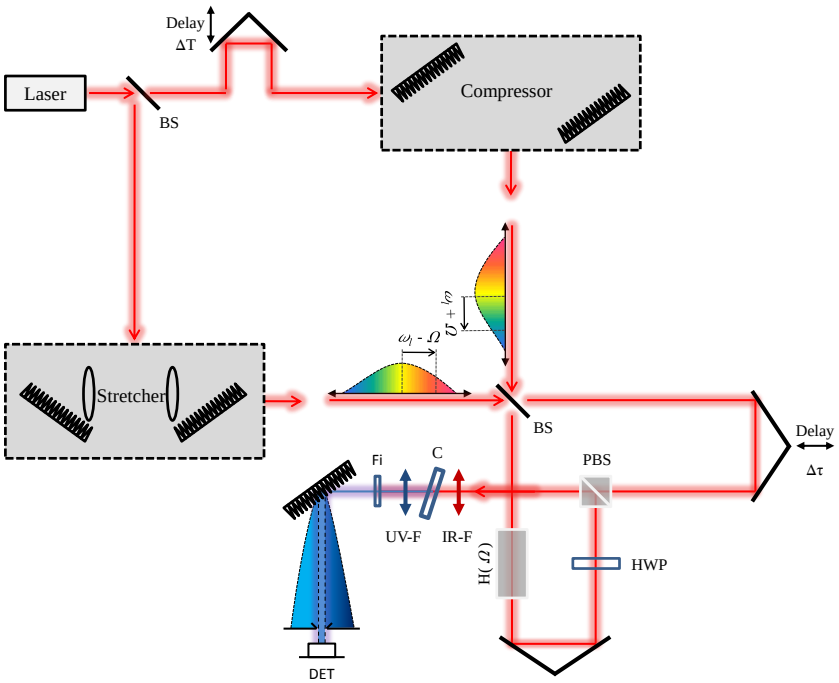

Figure 2.3: Experimental setup for chirped pulse interferometry. Up-chirped pulses from a gratings-based compressor and down-chirped pulses from a stretcher are combined at the 50/50 input beam splitter of our cross-correlator. The polarization is rotated with a half-wave plate (HWP) in the sample path from horizontal to vertical and collinear type-II SFG is employed. After spectral filtering, the CPI signal is measured with a photodiode (DET).

two arms is recombined at a polarizing beam splitter cube (PBS).

The output from the PBS is focused by a 5 cm achromatic lens onto a 0.5 mm BBO nonlinear crystal cut for collinear Type-II SFG. The sum-frequency beam is then recollimated by another 5-cm lens. Two dichroic mirrors designed to reflect 395 nm light and to transmit 790 nm light as well as a cyan-colored glass low-pass filter are used to filter the infrared light. These filtering elements are denoted as Fi in Figure 2.3. In order to filter a narrow-band of frequencies around $\sim 2\omega_l$, we use a combination of a diffraction grating and a slit. This way, most of the auto-correlation will be filtered out because of its broad bandwidth. The detected light is centered at 395.9 nm with a 0.4 nm bandwidth and the signal is measured using an amplified silicon photodiode.

2.3.2 Results and Discussion

CPI Interference

A SFG signal will only be generated if the delayed pulse overlaps temporally with the sample pulse at the BBO. The delayed pulse can either be an up-chirp (mixing with the down-chirp in the sample arm), or a down-chirp (mixing with the up-chirp in the sample arm). These different alternatives constitute the distributed Feynman paths, which can interfere. When the up-chirp is delayed by $\Delta\tau$ and is combined at the BBO with the down-chirp from the sample, the SFG instantaneous frequency is

$$\omega_{x_1}(\Delta\tau) = 2\omega_l - 2|\beta|\Delta\tau \tag{2.22}$$

and in the second case, we have

$$\omega_{x_2}(\Delta\tau) = 2\omega_l + 2|\beta|\Delta\tau \tag{2.23}$$

where β is the chirp rate. For large delays, the cross-correlation contains two different frequencies symmetric around $\sim 2\omega_l$. When $\Delta\tau = 0$, we see that $\omega_{x_1} = \omega_{x_2}$, and we observe CPI interference.

Figure 2.4(a) shows the result of measuring the SFG spectrum for different delays $\Delta\tau$. The spectrum units are wavelengths so that the cross-correlation line with a positive slope correspond the up-chirp being delayed ($\omega_{x_1}(\Delta\tau)$). The auto-correlation signal comprises a broad background barely visible in the figure.

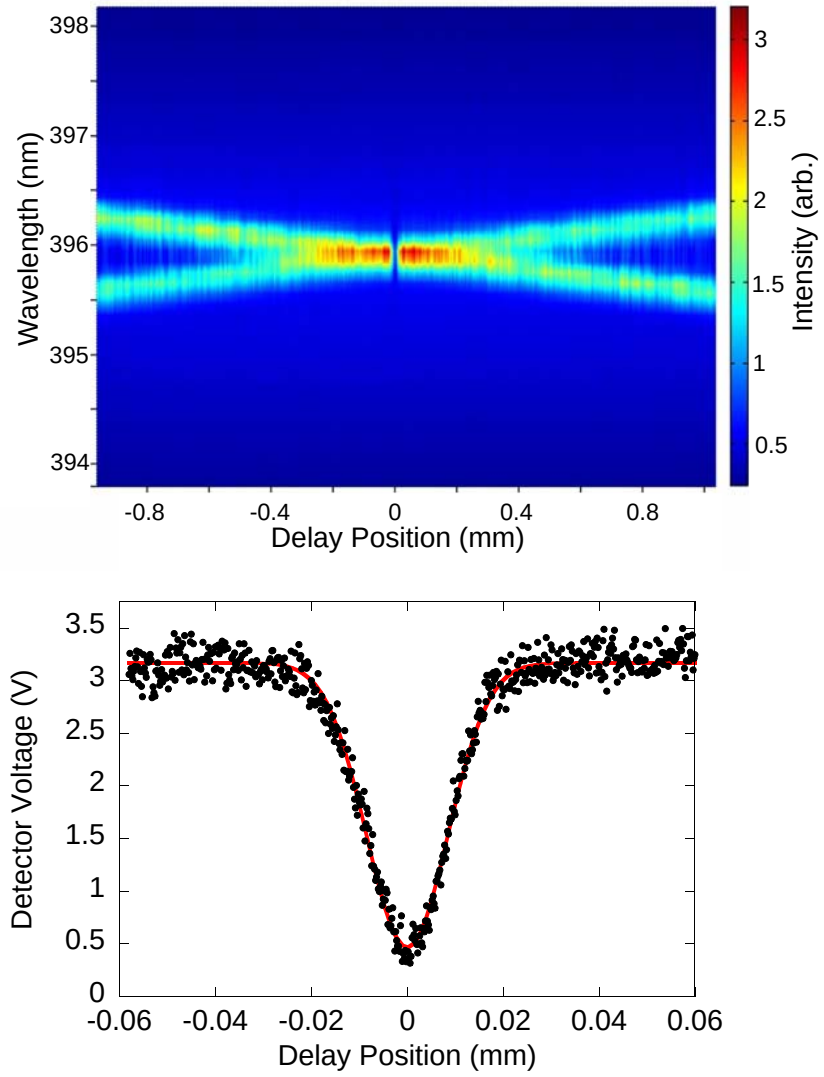

Figure 2.4: Experimental Chirped-pulse interference. a) Spectrum of the SFG versus delay position. We observe destructive interference between the cross-correlation signals near zero delay. b) Using a grating and a slit, we measure the optical power at 395.9 nm with a bandwidth of 0.4 nm, as function of delay. The signal shows a pronounced dip near zero delay; we use a Gaussian fit to measure the visibility (85.2 ± 0.6) % and width (19.9 ± 0.2) m FWHM.

It is also possible to measure the signal described by (2.5) with an amplified silicon photodiode when the spectral filtering, as described in the previous section, is employed. The photodiode signal as a function of delay is shown in Figure 2.4(b). The interference dip has a visibility[1] of 85.2±0.6 % and a full-width at half-maximum (FWHM) of 19.9±0.6 μm. The visibility is not perfect due to some residual background from the auto-correlations. The signal level of 3 V measured by our detector correspond to an optical power of 4.5 μW, or 10^{13} photons s^{-1}. This is 10 million times brighter than the highest reported coincidence rate from photon pair source [15]. This ratio does not take into account losses in the quantum interferometer and any reported detection rates in a full HOM interferometer are inevitably much lower.

Dispersion Cancellation and Group Delay

To demonstrate automatic dispersion cancellation, we took two data sets. The first one without dispersive material in the sample arm, and the second with 80.60 ± 0.05 mm of calcite and 28.93 ± 0.04 mm of BK7 glass. For each case, we measured CPI and white-light interferograms, for direct comparison, and the resulting interferomgrams are shown in Figure 2.5. To observe white-light interference, we placed a linear polarizer at 45^o before the nonlinear crystal. We used the up-chirp pulses as the light source and directly detected the transmitted infrared light.

Without sample (Figure 2.5(a)), we observe 143±2 fs FWHM for the CPI dip and 173± 1 fs FWHM for the white-light interference pattern. This corresponds to 17% difference in the resolution instead of the theoretical 29%. We attribute the difference between experiment and theory mainly to lost bandwidth in SFG. The dispersive elements inserted clearly increased the width of the white-light interference pattern by 75%, to 303 ± 2 fs FWHM (Figure 2.5(b)). However, we observe 140 ± 2 fs FWHM for CPI interference and the pattern didn't suffer from dispersion.

The centers of the interference patterns for both techniques have shifted due to the group delay. The measured delay when dispersive material is added corresponds to 34811.9± 0.3 μm for CPI and 34813.80 ± 0.3 μm. These agree with the theoretically predicted shift (cL/v_g) of 34816 ± 20 μm, calculated at 791.8 nm. Uncertainties in the theory result from errors in the measurement of sample thickness.

[1]Defined as $(I_{max} - I_{min})/I_{max}$

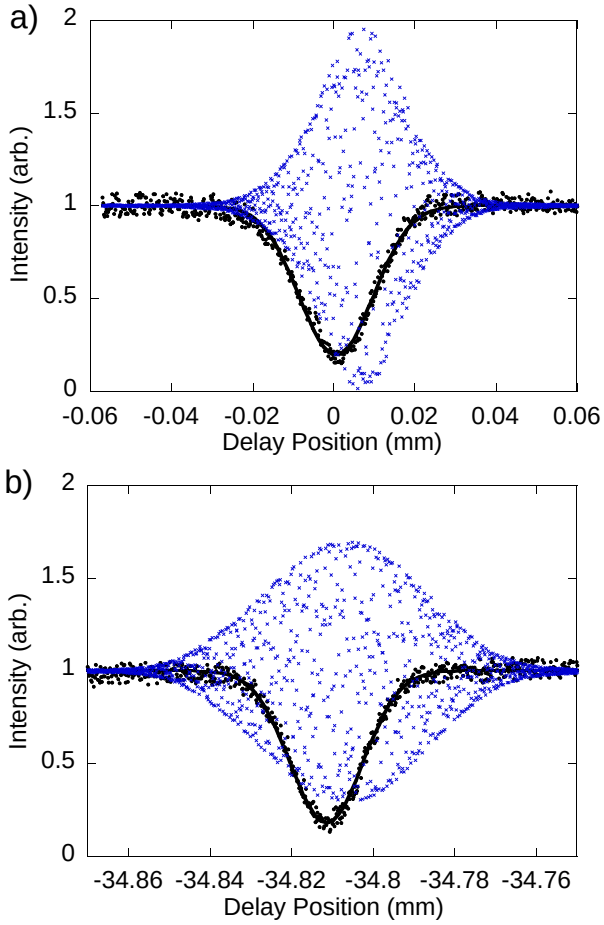

Figure 2.5: Automatic dispersion cancellation in chirped-pulse interferometry. These data show a direct comparison of the chirped-pulse interference signal (black circles) and standard white-light interference using the chirped pulse (blue x's) when a) no additional dispersive elements and b)(80.60 ± 0.05) mm of calcite (oriented for o-polarization) and (28.93 ± 0.04) mm of BK7 glass are placed in the sample arm. The white-light interferogram is broadened by 75% whereas the CPI interferogram shows no broadening. Even in the case of no dispersion, the CPI interferogram has 17% better resolution. Note that the small offset between the CPI and white-light interference is due to the birefringence of the up-conversion crystal.

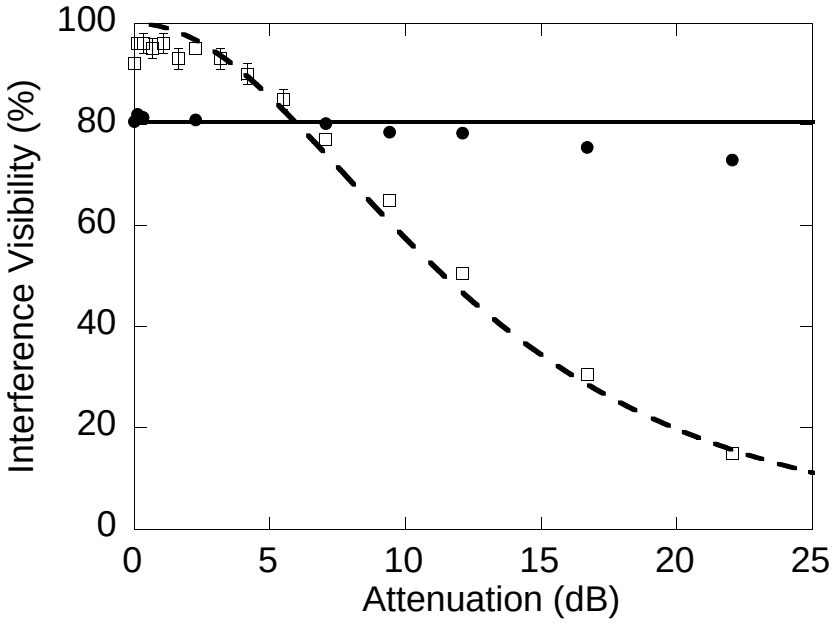

Figure 2.6: Visibility versus unbalanced loss. These data show the visibility of the chirped-pulse interference dip (closed circles, solid line theory) and white-light interference (open squares, dashed line theory) as a function of loss in the sample arm introduced by rotating the half-wave plate shown in Figure 2.3. The CPI dip visibility clearly shows its robustness against unbalanced loss. Error bars indicate statistical errors of 1 standard deviation and are not shown if smaller than the data point.

Like in HOM interference, the CPI signal's visibility is resilient to unbalanced loss in the interferometer arms. To illustrate this advantage over white-light interferometry, we measured the visibility for increasing loss in the sample arm. We achieve this by simply rotating the HWP in the sample arm, to control the amount of light reflected at the PBS. The visibility in CPI and white-light interference in function of attenuation is shown in Figure 2.6. The white-light visibility drops quickly with increasing loss, while the CPI visibility is only slightly affected. Deviations from the constant trend in CPI when significant attenuation is applied is attributed to the background, since it becomes more influential and reduces the signal-to-noise ratio.

2.3.3 Conclusion

We experimentally demonstrated CPI's ability to provide the same interferometric characteristics as those observed in HOM interference, relying on entangled photon-pairs. Additionally, CPI offers a signal level vastly higher than that of the quantum case, with state-of-the-art technology. The resilience to unbalanced loss and path-length fluctuations between the interferometer arms and immunity against even-order group-velocity dispersion are features unavailable in common white-light interferometry. CPI is therefore a promising alternative to optical imaging technologies, especially when dispersive and lossy materials are concerned.

Chapter 3

"Quantum-Optical Coherence Tomography" with Classical Light

In this chapter we demonstrate how to use CPI to measure axial interferograms to profile a sample accruing the important benefits of Q-OCT, including automatic dispersion cancellation, but with 10 million times higher signal. Our technique solves the artifact problem in Q-OCT and highlights the power of classical correlation in optical imaging.

Notice: The content of this chapter has been published: J. Lavoie, R. Kaltenbaek and K.J. Resch, Quantum-optical coherence tomography with classical light, Opt. Express, 17, pp. 3818-3825 (2009)

After we built and demonstrated the original CPI experiment in [16], my role was to modify the original setup to measure axial interferograms of a sample. I took all data, did all data analysis and wrote the first draft of the paper, including the figures (except for the false-color representation of the SFG spectrum, produced by RK). Finally, I worked with KR and RK to edit the final version.

3.1 Introduction

Optical coherence tomography (OCT) [17] is a non-invasive imaging technique using low-coherence interferometry to produce depth profiles of a sample. OCT has found many biomedical applications; prominent examples include the diagnosis of ocular diseases or detection of early-stage cancer [10]. Axial resolution in OCT is ultimately limited by the coherence length of the light source and can be less than 1 μm for very broadband sources [18]. This resolution is hindered by material dispersion which both broadens the features in the interferograms and reduces the contrast.

Exciting developments in quantum interferometry led to the proposal and demonstration of quantum-optical coherence tomography (Q-OCT) [9, 13]. This technique replaces white-light interferometry (WLI) with Hong-Ou-Mandel (HOM) interferometry [11] utilizing frequency-entangled photon pairs. This device automatically cancels all even orders of dispersion in the resulting interferogram, including group-velocity dispersion, the most significant contribution [12]. Dispersion cancellation in HOM interference is "blind", requiring no *a priori* knowledge of the material properties, in contrast with dispersion compensation methods (see [10] and references therein). In addition to dispersion cancellation, the HOM interferometer is phase insensitive, has better resolution than WLI with the same bandwidth, and the interference visibility is insensitive to unbalanced loss. Unfortunately, this technique is based on entangled photon pairs and the costs, in terms of speed and expense, have limited its widespread adoption. Other techniques for blind dispersion compensation without entanglement have been proposed [19, 20] or demonstrated [21], but they require unavailable technology [19] or significant numerical post-processing [20, 21] and do not have the other advantageous properties of Q-OCT. We have recently demonstrated a completely classical technique, based on oppositely-chirped laser pulses, for producing an interferogram with *all* the advantages of HOM interference with vastly higher signal [16].

In the present work, we use chirped-pulse interferometry (CPI) for axial profiling a sample with two optical interfaces. Q-OCT interferograms have been shown to contain artifacts [9], signals that do not correspond to real features of the sample. Due to the strong analogy, these artifacts also appear in CPI-based axial imaging. We experimentally demonstrate a straightforward method for controlling these artifacts. Although it is possible to control these artifacts in Q-OCT as well [9], it is technically challenging and has not been demonstrated.

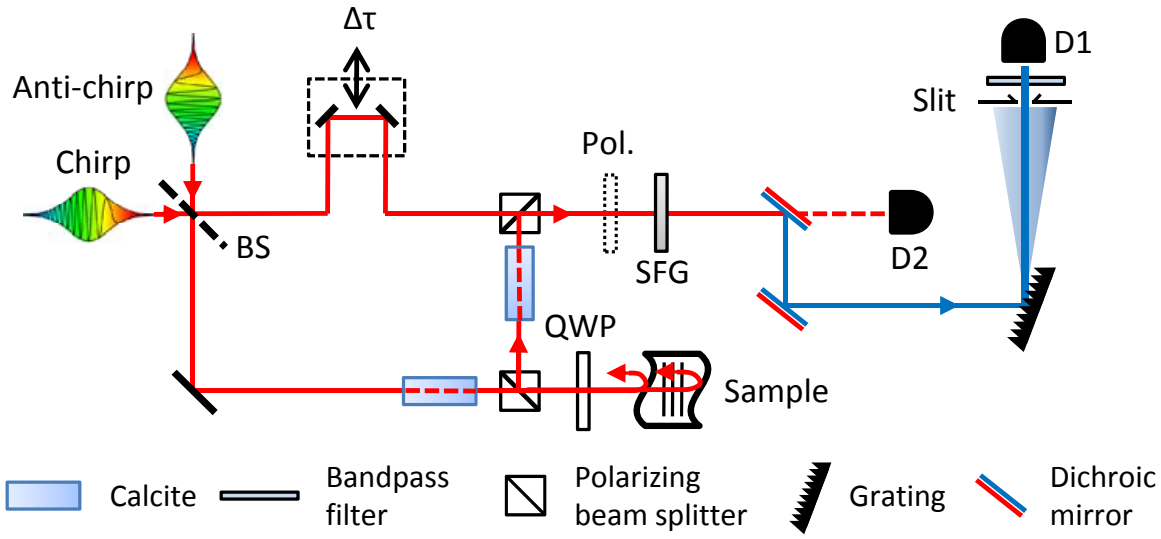

Figure 3.1: Experimental setup for axial profiling with chirped-pulse interferometry. Pairs of oppositely-chirped laser pulses with horizontal polarization are combined at a 50/50 beam splitter (BS). The light from one BS output reflects from a sample; the light from the other undergoes a spatial delay. In the sample arm, two passes through the quarter-wave plate (QWP) rotate the polarization to vertical. This allows spatial recombination of the two beams at a polarizing beam splitter. Both beams are focussed onto a 0.5 mm thick BBO crystal phase-matched for type-II sum-frequency generation (SFG). Dichroic mirrors separate the fundamental from the SFG light. A grating and slit are used to filter a narrow band (0.46 nm FWHM) of SFG light before the light is detected by an amplified Si photodetector (D1). An alternate configuration, where a 45° polarizer is inserted before the nonlinear crystal and the fundamental light is directly detected with a photodiode (D2), allows the observation of white-light fringes and a direct comparison with CPI. A pair of calcite blocks can be inserted to compare the effects of material dispersion on the interferograms.

3.2 Experimental Setup and Methods

Our interferometer is shown in Fig. 1 and described in the caption. It relies on pairs of oppositely-chirped laser pulses that have been stretched to several hundred times their initial, transform-limited, pulse duration. In this large-chirp limit, at any given time the two frequency-anticorrelated pulses have frequencies $\omega_0 + \Omega$ and $\omega_0 - \Omega$, respectively. Here, ω_0 is the average of the instantaneous frequencies of these pulses. If the chirped pulses are coincident at the input beam splitter, ω_0 is equal to the centre frequency of the laser, but it can be tuned by changing the relative delay between the pulses. We refer to ω_0 as the *operating frequency* to distinguish it from the centre frequency of the laser. Following the theoretical framework from [9], we assume that the effect of the sample is modelled by a linear transfer function, $H(\Omega)$. The reference arm contains an adjustable path delay, $\Delta\tau$. After propagation in each arm, the beams undergo sum-frequency generation (SFG) in a nonlinear medium. We detect SFG light in a very narrow frequency band near $2\omega_0$ ensuring that the output signal is almost exclusively due to cross-correlations between the chirped and anti-chirped pulses. Under these conditions, the signal integrated over all frequencies in the chirped pulses and measured by a square-law detector, $S(\Delta\tau)$, is

$$S(\Delta\tau) \quad \propto \quad \int d\Omega I(\Omega) I(-\Omega) |H(\Omega)|^2 - \mathrm{Re}\left[\int d\Omega I(\Omega) I(-\Omega) H(\Omega) H^*(-\Omega) e^{-2i\Omega\Delta\tau} \right] \quad (3.1)$$

where $I(\Omega)$ is the intensity spectrum of both laser pulses. The CPI signal is identical to that in Q-OCT when $I(\Omega)I(-\Omega)$ is equal to the spectrum of the entangled photons (see [9], Eqns. (6)-(8)).

A mode-locked Ti:Sapphire laser (center wavelength 790 nm, average power 2.7 W, repetition rate 80 MHz) was used to create a pair of horizontally-polarized beams of oppositely-chirped pulses using a grating-based stretcher and compressor [22]. These stretched the initial pulses from 100 fs to 54 ps (48 ps) with 11 nm (10 nm) bandwidth for the chirped (anti-chirped) pulses. Note that the difference in the pulse duration is due to slightly different bandwidths, not different chirp rates. Details on the stretcher and compressor can be found in [16].

3.3 Results and Discussion

We used a borosilicate microscope coverglass as the sample. The CPI (WLI) data was taken by recording the signal of detector D1 (D2) over the delay $\Delta\tau$. In each scan data was accumulated for 0.5 s over a range of 0.5 mm. The data without and with the calcite blocks are shown in Fig. 2(a) and Fig. 2(b), respectively, where the upper (lower) plots are CPI (WLI) scans. Without additional dispersion (Fig. 2(a)), the CPI interference dips have widths of 20.1±0.3 μm and 20.6±0.4 μm FWHM and corresponding visibilities of 39.0% and 40.9% for the front and the back surface of the coverglass, respectively. The WLI patterns have widths 30.4±0.3 μm and 29.9±0.3 μm FWHM and corresponding visibilities of 12.9% and 14.0%. The errors in these measurements are mainly due to positioning uncertainty of the motor. Even without the addition of calcite blocks, we see that the CPI signal has enhanced resolution by a factor of 1.5 compared to WLI. This enhancement factor is slightly larger than the theoretically expected value of $\sqrt{2}$ (assuming Gaussian spectra), due to uncompensated dispersion caused by the additional PBS in the sample arm.

The average optical power in the WLI scans in Figs. 2(a) & 2(b) was ∼10 mW. In the CPI scans, the normalized intensity of 1.0 corresponds to 0.3 μW of measured optical power. This corresponds to approximately 10^{12} photons/s. It is difficult to directly compare this rate with the performance of Q-OCT demonstrated in [13] since only normalized rates are presented; however, the highest measured coincidence-counting rate from an entangled photon source to date is $\sim 10^6$ photons/s [15]. Given a total sample reflectivity of $\sim 10\%$ our measured power is 7 orders of magnitude larger than what could be achieved in Q-OCT with the best available technology.

The path delay between the two CPI interference dips is 286.1±0.4 μm. The operating frequency was measured by taking the spectrum of the light after the first beam splitter; it is the frequency at which the chirped and antichirped pulses interfere. The observed delay can be converted to the thickness of the coverslip by dividing by the group index, $n_g(\lambda) = n(\lambda) - \lambda \left.\frac{dn}{d\lambda}\right|_\lambda$, of borosilicate glass at the operating wavelength 790.8±0.3 nm, $n_g = 1.53482$ [23]. The optical measurement of the coverglass thickness is 186.4 ± 0.3 μm which is in good agreement with a direct measurement, using a micrometer, yielding 186.4 ± 0.8 μm.

To investigate the effects of material dispersion on the interference, we added a pair of calcite beam displacers into the setup. The sum of their lengths is 80.58±0.01 mm and the

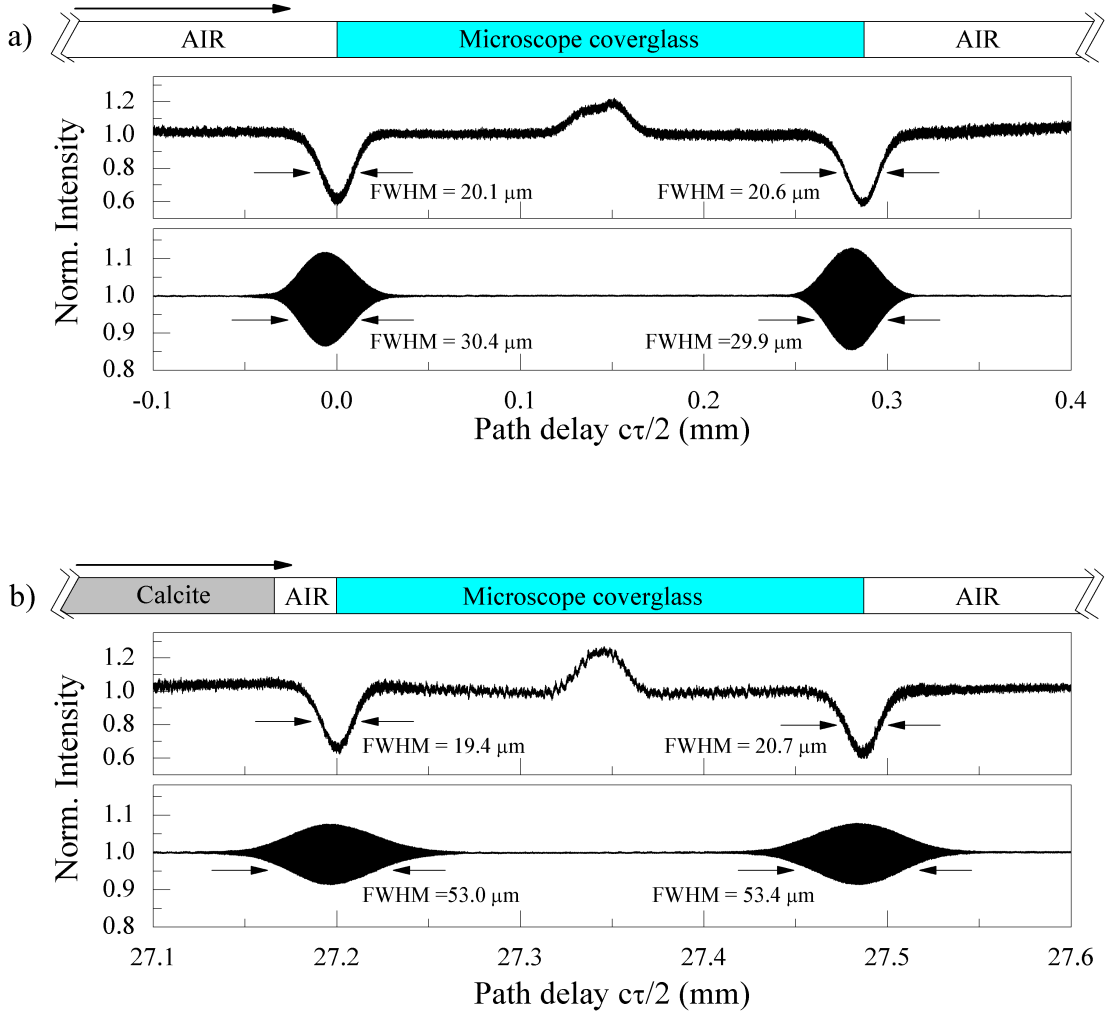

Figure 3.2: Axial scans of a microscope coverglass using chirped-pulse and white-light interference. Light enters from the left and is reflected from either the front or the back surface of the sample, as indicated at the top of the figure. The normalized detector signal is plotted as a function of path delay. Each data set shows interference features corresponding to the front and back surface reflections of the sample. The CPI (top) and the WLI (bottom) were taken a) without and b) with calcite blocks. The CPI signal resolution, as measured by the width of the interference feature, is unaffected by the dispersion whereas the WLI is broadened by 74%. As in Q-OCT, CPI shows an artifact between the two real signals.

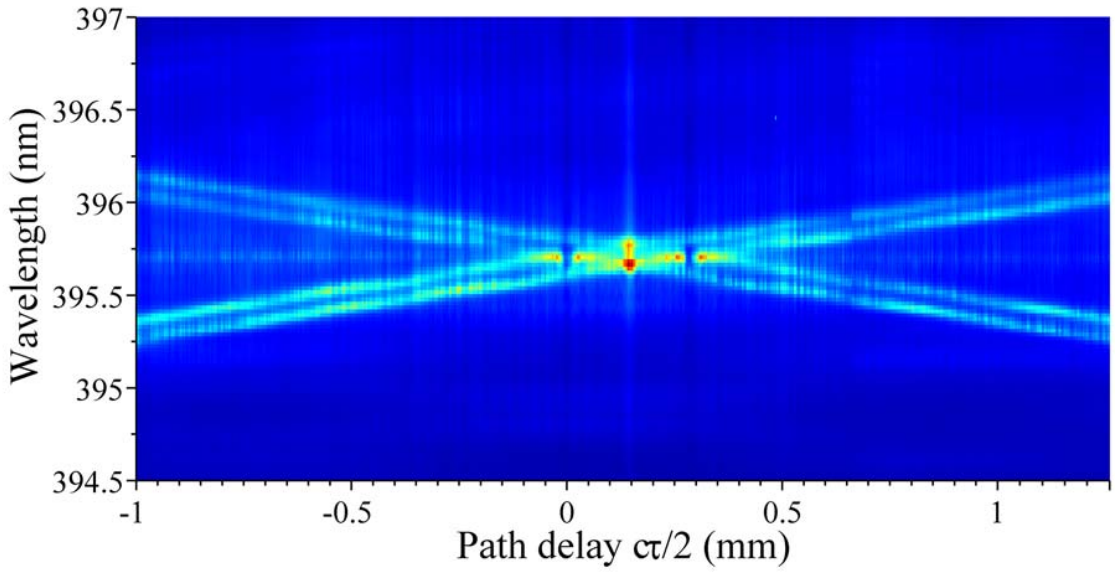

Figure 3.3: False-color representation of the SFG spectrum vs path delay. Two pairs of narrow lines originate from SFG of the oppositely-chirped laser pulses with different time delays. When the time delay through the reference arm coincides with the delay through the sample arm from one of the two interfaces, an interference dip occurs. The other pair of crossings between the real interference dips gives rise to the artifact.

light propagates through them with ordinary polarization. The widths of the CPI dips are unchanged at 19.4±0.6 μm and 20.7±0.4 μm FWHM; the WLI envelopes are significantly broadened by 74% to 53.0±0.3 μm and 53.4±0.3 μm. Under these conditions, CPI has a factor of 2.65 better resolution than WLI.

Both CPI and Q-OCT signals contain artifacts, additional features in the interferograms that do not correspond to real interfaces. These can be seen in the data in Fig. 2 in between the interference dips. To illuminate the origin of these features in CPI we measured the full SFG spectrum as a function of delay using a high-resolution spectrometer (ACTON SP-2758). The results are shown in Fig. 3. On this scale, the only features visible are due to cross-correlations; the autocorrelations form a weak, broadband background. When the paths are unbalanced, the signal contains two doublets of narrow spectral lines. One of these doublets is due to the chirped pulse traversing the sample arm and the anti-chirped pulse traversing the reference. The two peaks of the doublet are separated in frequency due to the difference in optical delay reflecting from the front and back surface of the sample. When the chirped pulse is reflected from the front surface the frequency of the cross-correlation will be slightly higher than upon reflection from the back surface. The other doublet can be understood by swapping the roles of the chirped and anti-chirped pulses.

Changing the path delay changes the spacing between the two doublets. An interference dip occurs when the delay in the reference path is equal to a delay in the sample path. The interference results from two different processes (chirp in one of the two arms and anti-chirp in the other) each producing light at the same frequency, but out of phase. In Fig. 3 the four lines, formed by the two doublets for varying path delay, cross at four distinct points. Two of these points occur at the same wavelength but at different path delays; they correspond to the dips in the CPI scans indicating real features of the sample. The other two crossing points occur at the same path delay but different wavelengths; these give rise to the artifacts.

As in Q-OCT, the interference giving rise to the artifacts can be constructive or destructive whereas for real features it is always destructive. If the interference is constructive, as in Fig. 2, the artifact is easy to identify. If instead it is destructive, artifacts can easily be confused with real features. In Q-OCT it was predicted that this could be adjusted by changing the sum-frequency of the entangled photon pair [9]. In practice, however, this is difficult as most UV narrow-band pump sources for SPDC are not tunable. CPI has

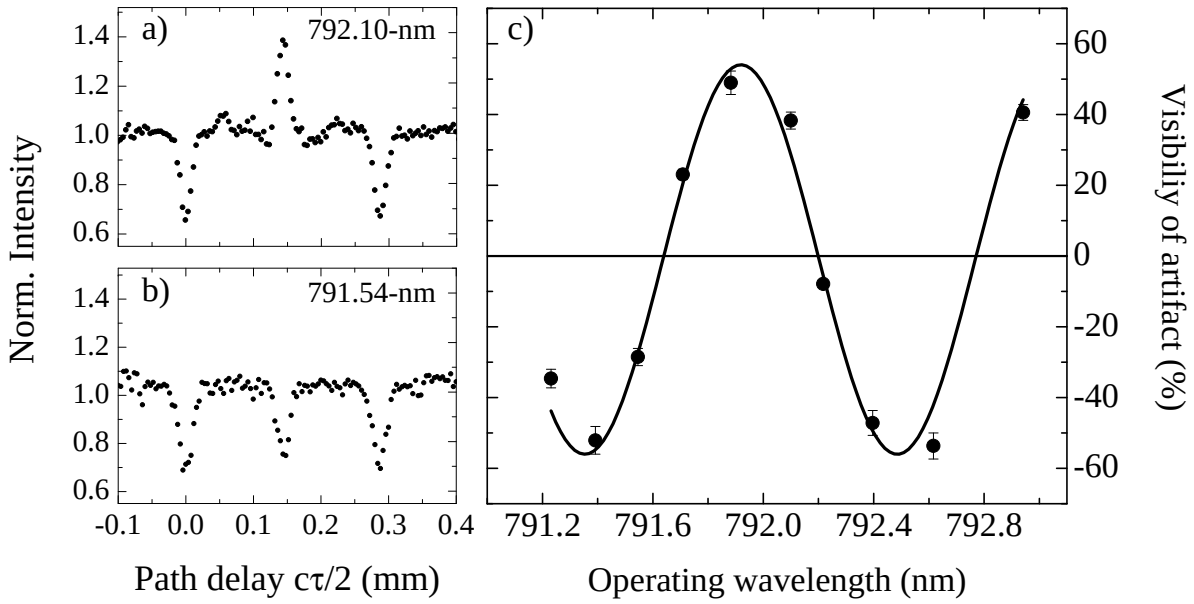

Figure 3.4: Controlling the phase of the artifact. CPI interferograms of the sample taken at an operating wavelength of a) 792.10 nm and b) 791.54 nm clearly shows the dependence of the phase of the artifact interference on the operating wavelength. c) Visibility of the artifact versus operating wavelength. Positive (negative) visibility corresponds to constructive (destructive) interference. The measured period of oscillation of (1.13±0.02) nm is in good agreement with the theoretical expectation.

the intrinsic advantage that the operating frequency is tunable by changing the relative delay between the chirped and anti-chirped pulses at the input beam splitter. In Figs. 4(a) and 4(b), we show two examples of CPI interferograms taken at different operating wavelengths 792.10 nm and 791.54 nm illustrating constructive and destructive interference in the artifact, respectively. The operating frequency is half the SFG frequency measured near zero delay. In these scans the path delay was not varied continuously but in discrete steps, accounting for fewer data points.

We employ the model transfer function for the coverslip, $H(\Omega) = r_1 + r_2 e^{i2k(\omega_0+\Omega)d}$, where r_1 (r_2) is the reflection amplitude from the front (back) surface, $k(\omega)$ is the wavevector in the glass, and d is the thickness. Inserting this expression into Eq. (1), one finds that the term describing the artifact is modulated by $\cos 2k(\omega_0)d$. If the operating frequency changes from ω_0 to $\omega_0 + \delta$, then $k(\omega_0 + \delta) \approx k(\omega_0) + \alpha\delta$ and the expected change in wavelength required to flip the sign of the artifact is $\Delta\lambda \approx \pi^2 c/(\omega_0^2 \alpha d)$.

Figure 4(c) shows the visibility of the artifact as a function of the operating wavelength. Visibility is defined as $(I_C - I_S)/I_S$, where I_C and I_S are the intensities at the centre of the dip and at the shoulder, respectively. A fit to this data yields a period of (1.13±0.02) nm in good agreement with the theoretical prediction of 1.09 nm. Changing the operating wavelength in this straightforward way allows identification and removal of artifacts from axial scans.

There is a difference between Q-OCT and CPI. Even in the absence of dispersion, the resolution in Q-OCT is a factor of 2 better than in WLI [9] while, assuming Gaussian spectra, CPI has a factor of $\sqrt{2}$ better resolution than WLI. The difference originates from the effective bandwidths used in the comparison. Assuming a source of entangled photons with spectrum $S(\Omega)$ (the modulus squared of $\zeta(\Omega)$ in Eq. (5) in [9]), the effective bandwidths for HOM interference (see [9], Eq. (8)) and WLI (see [9], Eq. (4)) are the same because their spectra, $S(\Omega)$, are identical [24]. For chirped pulses with spectra $I(\Omega)$, the bandwidth for CPI is determined by $I(\Omega)I(-\Omega)$ (see Eq. (1)) while that for WLI is determined by $I(\Omega)$. For Gaussian spectra the effective bandwidth for CPI is $\sqrt{2}$ narrower than that for the WLI, accounting for the resolution advantage of Q-OCT.

Is this a fundamental feature of entanglement? Surprisingly no. The same difference in resolution could be achieved using purely classical correlations. In CPI, time-correlations, but not intensity correlations are created between anticorrelated frequencies. In the same

setup, one replaces the chirped pulses with two CW lasers tuned to frequencies $\omega_0 + \Omega$ and $\omega_0 + \Omega'$. During the integration time of the detection the laser frequencies are swept in an anticorrelated way according to the distribution $P(\Omega, \Omega') = G(\Omega)\delta(\Omega + \Omega')$. In this case, the effective spectrum in Eq. (1) is $G(\Omega)$, while the WLI bandwidth is determined by the marginal $P(\Omega) = \int d\Omega' P(\Omega, \Omega') = G(\Omega)$. The effective bandwidths are identical in both cases and thus this classical scheme achieves the same factor of 2 higher resolution as Q-OCT. In practice, however, chirped pulses offer dramatically higher nonlinear conversion efficiency compared to CW lasers far outweighing this rather small difference.

3.4 Conclusion

We have shown that chirped-pulse interferometry accrues the benefits of quantum-OCT, but with a dramatic increase in signal, direct optical detection, and a straightforward means of identifying artifacts. We have experimentally demonstrated improved resolution in CPI over WLI with and without mismatched dispersion by up to a factor of 2.65. Increasing the bandwidth of the light source is required for the resolution in CPI-based OCT to compete with established techniques. Broadband (148nm) three-wave mixing of anticorrelated frequencies has been demonstrated in 1.5mm-thick nonlinear materials [25]. For safe *in vivo* imaging, the optical power can be attenuated before the sample without loss of signal visibility [16]. We have demonstrated SFG detection of reflected signals as low as 5mW [16]. Based on the results of [26], efficient SFG should be measureable with much lower reflected powers. Incorporating better nonlinear materials, such as PPKTP, and more sensitive detectors will further allow operation at lower power levels. CPI achieves the benefits of quantum interferometry at macroscopic power levels and represents a powerful new technique for optical imaging. More generally, we have clarified the role of entanglement versus correlation in axial imaging.

Chapter 4

Classical Analogues of Two-Photon Quantum Interference

Chirped-pulse interferometry (CPI) captures the metrological advantages of the quantum Hong-Ou-Mandel (HOM) interferometry in a completely classical system. Modified HOM interferometers are the basis for a number of seminal quantum interference effects. In this chapter, we show how the corresponding modifications to CPI allow for the first observation of classical analogues to the HOM peak and quantum beating. They also allow a new classical technique for generating phase super-resolution exhibiting a coherence length dramatically longer than that of the laser light, analogous to increased two-photon coherence lengths in entangled states.

Notice: The content of this chapter has been published: R. Kaltenbaek, J. Lavoie and K.J. Resch, Classical analogues to two-photon interference, Phys. Rev. Lett. 102, 243601 (2009)

My role was to prepare the experimental setup, from our previous configuration [16]. I performed the original measurements to demonstrate constructive interference in CPI and spatial beating and analyzed the corresponding data. The first attempts for phase super-resolution failed since the motor step size could not resolve the interferometric fringes. RK changed the acquisition technique and succeeded in demonstrating the signature of phase super-resolution. RK wrote the first draft of the paper and I worked with KR and RK to

edit the final version.

4.1 Introduction

Quantum-optics experiments demonstrated a wide range of interference phenomena that had never before been seen in classical systems. Prominent examples include: automatic dispersion and aberration cancellation [12, 27, 28], phase-insensitive interference [11], nonlocal interference [29, 30], ghost imaging [31] & ghost diffraction [32], phase super-resolution [33, 34, 35], and phase super-sensitivity [36, 37, 38, 39]. Some of these phenomena form the basis for applications in quantum computing and metrology that promise to outperform their classical counterparts in terms of speed and precision, respectively. Recently, ghost imaging [40, 41], automatic dispersion cancellation [21, **?**, 42], phase super-resolution [43], and phase insensitive interference [**?**] have been observed in classical optical systems exploiting correlation, but not entanglement. Chirped-pulse interferometry (CPI) [**?**] is a new, completely classical technique producing the same interferogram as a Hong-Ou-Mandel (HOM) interferometer [**?**] based on frequency-entangled photon pairs, but with vastly higher signal. It has been shown that modifications to the HOM interferometer can produce a wide array of quantum interference effects such as the HOM peak [44], quantum beating [45, 46], and phase super-resolution [33]. In the present work, we show how similar modifications to CPI can produce the analogous interferometric signatures with only classical resources. Thus we rule out the HOM peak and quantum beating signatures as uniquely quantum and demonstrate phase super-resolution in a classical context with important differences from previous work [43].

Hong-Ou-Mandel interference [**?**] is ubiquitous in optical quantum information processing, underlying such effects as quantum teleportation [47, 48] and linear-optics quantum computation [49]. It occurs when two photons are coherently combined on a beamsplitter, and manifests as a dip in the coincidence rate of two detectors. A typical HOM interferometer, apart from the bandpass filters, is depicted in Fig. 4.1b) (upper). HOM interference with frequency-entangled photons exhibits automatic dispersion cancellation, phase insensitivity and robustness against loss, rendering it a promising tool for quantum metrology and imaging techniques [**?**, **?**, **?**]. We have recently demonstrated chirped-pulse interferometry [**?**], a completely classical interferometer whose output exhibits all of these important

features of HOM interference. This classical approach can be viewed as a time-reversed version of the HOM interferometer [43], see Fig. 4.1b) (middle). Instead of down-converting a narrow frequency photon and detecting photons with anticorrelated frequencies, we prepare light with anticorrelated frequencies and detect a narrow frequency band. The CPI setup can be seen in Fig. 4.1b) (bottom) where a pair of oppositely-chirped laser pulses enter into a cross-correlator. A narrow bandwidth of the output sum-frequency generation (SFG) is detected on a standard photodiode as a function of the time delay, $\Delta\tau$. We have shown that CPI can be used in place of HOM interference to obtain the same benefits of quantum-optical coherence tomography [**?**] with dramatically larger signal and a straightforward means of control over intrinsic signal artifacts [42].

Several quantum-interference effects are based on modifications of the HOM interferometer, such as the three shown in Figs. 4.1a)-c) (upper). In Fig. 4.1a) photon pairs are detected in one output. The photon bunching leading to the HOM dip gives rise to phase-insensitive constructive interference, a *HOM peak*, in the coincidence rate of these detectors [44]. In Fig. 4.1b) bandpass filters centred at different wavelengths are placed before the detectors. The coincidence rate in this device exhibits phase-sensitive interference, but at a wavelength that depends on the frequency difference of the filters [45, 46]. The wavelength of the interference, referred to as *quantum beating*, can be much longer than the wavelength of the light. In Fig. 4.1c) the output of the HOM is fed into a Mach-Zehnder interferometer. The output of the first interferometer can be approximated by a two-photon NOON state, $|\psi\rangle \sim |2\rangle|0\rangle + |0\rangle|2\rangle$, which exhibits *phase super-resolution* (PSR), manifesting as a wavelength of interference two times shorter than that of the light passing through the interferometer.

4.2 Experimental Setup and Methods

For the experimental realization of classical analogues of these three quantum effects, we use a modelocked ti:sapphire laser (centre wavelength 790 nm, pulse duration 100 fs FWHM, average power 2.8 W, repetition rate 80 MHz) as the light source. The beam is split at a 50:50 beam splitter. Its two outputs pass through a grating-based stretcher [4] and compressor [2] to generate chirped pulses approximately 54 ps long and anti-chirped pulses 48 ps long (FWHM), respectively. The difference in pulse durations is due to slightly different

bandwidths rather than different chirp rates. Because the stretcher and the compressor are aligned to generate an equal but opposite chirp rate, at any given time the sum of the instantaneous frequencies of the two pulses is constant. For more details, see [**?**].

Fig 4.1b)(lower) shows the basic CPI setup. The horizontally-polarized chirped and antichirped beams are combined at a 50:50 beam splitter. From there the outputs travel along two different spatial paths, one of which contains an adjustable path delay. The polarization in one of the paths is rotated to vertical by a half-wave plate. This allows the recombination of the beams into a single spatial mode, but with orthogonal polarizations, at a polarizing beam splitter. That mode is focused onto a 0.5 mm thick type-II phase-matched β-Barium Borate crystal for SFG. High-pass filters separate the SFG from the fundamental signal. A narrow bandwidth of the SFG is filtered using gratings and a slit and is detected using an amplified Si photodiode (Thorlabs PDA36A).

4.3 Results and Discussion

The HOM peak can be observed in the quantum interferometer shown in Fig. 4.1a) (upper). Time-reversing this setup requires combining the oppositely-chirped laser pulses at a beamsplitter before the input to the cross-correlator as shown in Fig. 4.1a) (middle). Fig. 4.2a) shows the resulting interferogram as a function of delay. The path length was varied in the delay arm of the cross-correlator by moving a motor with a constant velocity of 0.500 ± 0.005 mm/s. Simultaneously, data was acquired with a sample rate of 12 kHz. The gratings and the slit were adjusted to filter the SFG with a bandwidth of 0.4 nm FWHM around the center wavelength 395.2 ± 0.1 nm. The sole feature in the interferogram is a phase-insensitive constructive interference peak with visibility $76 \pm 2\,\%$. In Ref. [50] it was shown that an absorber that removes a narrow portion of the spectrum near the centre frequency ω_0 in front of the single-photon detectors leads to a reduced coincidence rate close to the HOM peak. This feature can be interpreted as enhanced absorption through a photon exchange effect. In our experiment, we achieve an analogous signal by blocking a 2.0 ± 0.3 nm band of the spectrum at the centre frequency by placing an Allen key in the beam inside the stretcher. Fig. 4.2b) is the resulting interferogram clearly showing the appearance of two dips for delay positions just outside the peak.

Quantum beating was originally observed in the quantum interferometer shown in

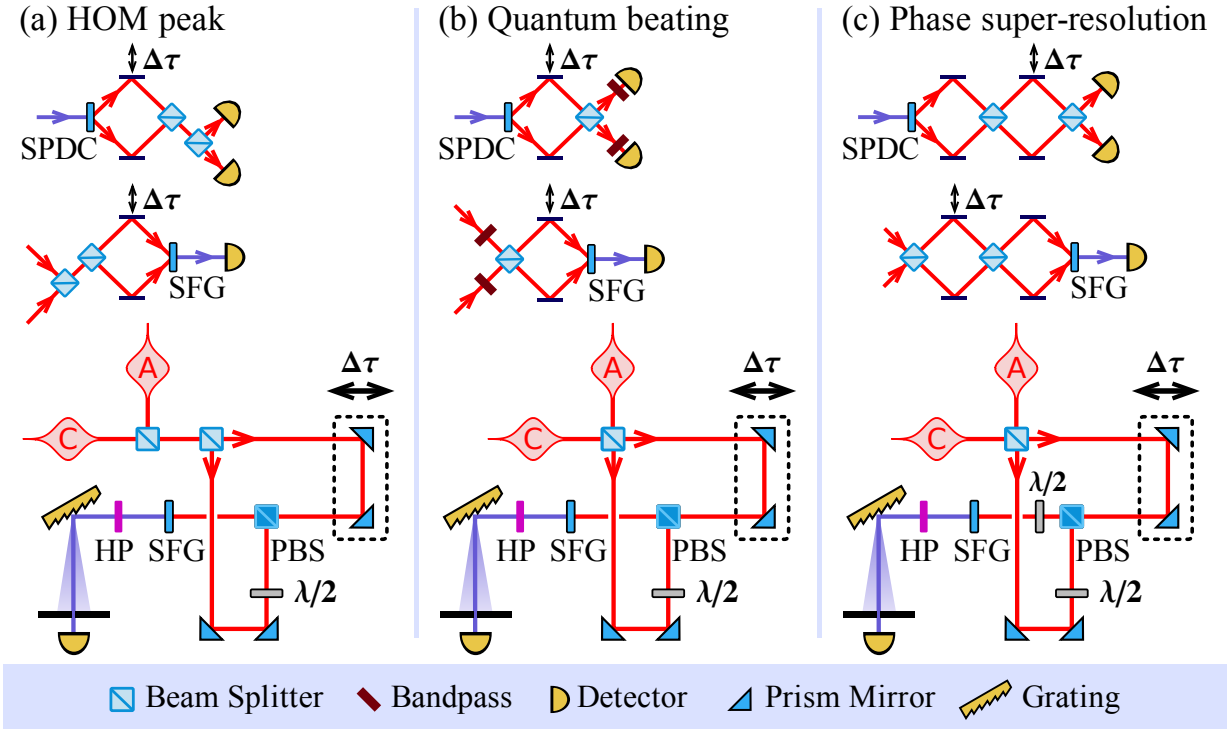

Figure 4.1: Two-photon interferometers and their time-reversed analogues. The three top figures show schematic of the quantum interferometers used to observe a) the HOM peak, b) quantum beating (note the inclusion of two filters with different bandpasses), and c) two-photon phase super-resolution. All of the interferometers rely on light created from spontaneous parametric down-conversion (SPDC) in a nonlinear crystal. The interferograms correspond to the number of coincidence counts registered at a pair of photon counting detectors as a function of the path delay, $\Delta\tau$. The middle row of figures depict the time-reversed version of each quantum interferometer based on the recently described chirped-pulse interferometry [**?**]. These time-reversed interferometers were implemented as shown in the bottom row of figures. Chirped (C) and and anti-chirped (A) laser pulses with matched chirp rates are combined at the inputs of the interferometers. The light passes along the two arms of the interferometer, is recombined at a polarizing beam splitter (PBS), and is focused on a nonlinear crystal. High-pass filters (HP) remove the fundamental from the resulting sum-frequency generation (SFG). A narrow band of frequencies is filtered, via gratings and a slit, and detected via an amplified Si photodiode.

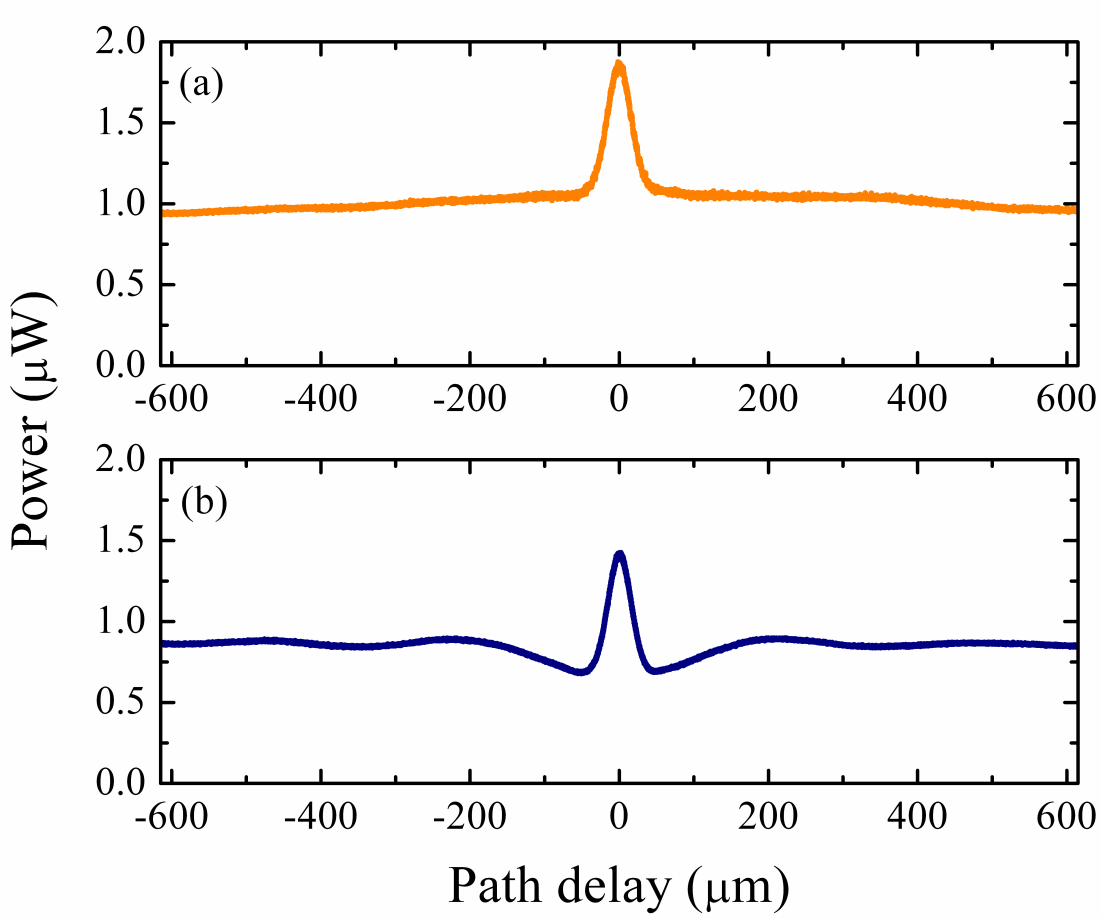

Figure 4.2: Phase-insensitive constructive interference in CPI. The system was set up as depicted in Fig. 4.1a) (bottom) as the time-reversed version of the two-photon interferometer in Fig. 4.1a) (top). In b) the configuration was the same as in a) except that we blocked 2.0 ± 0.3 nm near the centre wavelength of the chirped pulses in the stretcher. Both plots show the measured photodiode signal as a function of delay. The data in a) shows a phase-insensitive interference peak with visibility $76 \pm 2\,\%$ and FWHM 42 ± 2. The data in b) shows a peak with similar visibility and width, but with two new features where the signal drops at +/-$50 \pm 4\,\mu$m by $20 \pm 1\,\%$ of the plateau signal level.

Fig. 4.1b)(upper) [45]. This is a standard HOM interferometer where interference filters with different bandpasses are placed in front of the detectors *after* the interferometer. Time-reversing this setup requires filtering different bandwidths of the chirped and anti-chirped beams *before* the interferometer. We inserted razor blades into the stretcher and compressor to block spectral components of the light. The measured spectra for two different positions of the razor blades are shown in Figs. 4.3b) and d). We measured the SFG signal as a function of delay by moving a motor in the delay path in steps of $3\,\mu$m. Note that in this configuration we used a stepper motor and took data at discrete positions, whereas for the other data we moved the motor and took data continuously. This accounts for the qualitative difference between the appearance of these data sets and the others. The SFG signal was detected within a bandwidth of $0.3 \pm 0.1\,$nm FWHM around $394.5 \pm 0.1\,$nm.

The resulting CPI interferograms as functions of path delay are shown in Figs. 4.3a) and c). Both signals clearly exhibit interference fringes but with periods much larger than the wavelength of the light. This is the same characteristic feature that was oberved in the quantum beating experiment [45, 46]. For Figs. 4.3a) and c) the difference frequency, as determined by the peaks of the spectra, between chirp and anti-chirp is $17 \pm 1\,\mathrm{ps}^{-1}$ and $45 \pm 1\,\mathrm{ps}^{-1}$, respectively. From these difference frequencies, we expect the corresponding fringe spacings to be $111 \pm 7\,\mu$m and $42 \pm 1\,\mu$m. Both are in good agreement with the measured fringe spacings, $115 \pm 15\,\mu$m and $40 \pm 2\,\mu$m, and much larger than either the wavelength of the SFG, $0.395\,\mu$m, or the chirped pulses, $0.790\,\mu$m.

Two-photon phase super-resolution can be observed in the interferometer shown in Fig. 4.1c) (upper). The output of a balanced HOM interferometer is fed into a Mach-Zehnder interferometer. HOM interference causes photon pairs to bunch together, creating number-path entangled states. These exhibit interference fringes, as measured in the coincidence rate of the detectors, at half the classical period. For the time-reversed version, one could employ a spatial encoding as depicted in Fig. 4.1c) (middle). However, we used an equivalent transformation on the polarization degree of freedom by simply inserting a half-wave plate, oriented at 22.5°, before the SFG as shown in Fig. 4.1c) (bottom).

Figs. 4.4c) & d) show the results of a continuous scan of the SFG signal over the path delay in the cross-correlator. For comparison, Figs. 4.4a) & b) show a white-light interferogram taken by replacing the half-wave plate with a polarizer at 45° and measuring the fundamental light with a fast photodiode (Thorlabs DET100A). In both cases, the path

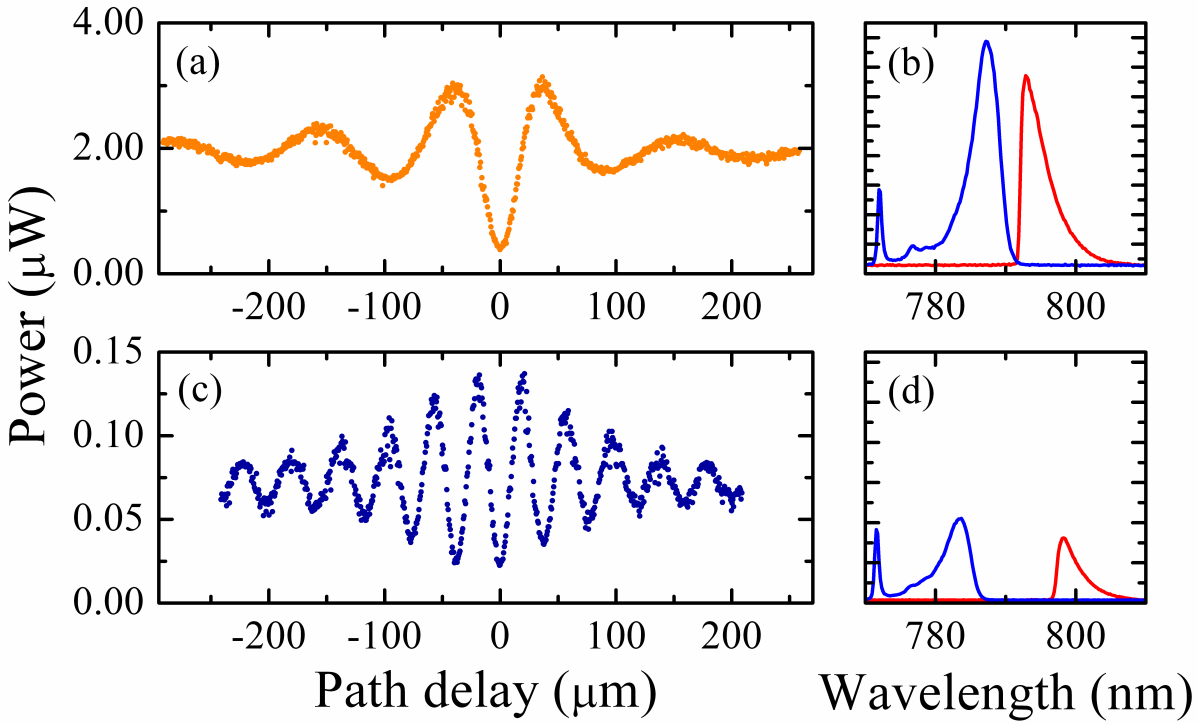

Figure 4.3: "Quantum" beating in CPI. Filtering different spectral components of the chirped and anti-chirped input plays the same role in CPI as filtering different spectral components in the HOM interferometer Fig. 4.1b) (top). Measured interference patterns a) and c), and the corresponding spectra of the chirped (red) and anti-chirped (blue) beams b) and d), respectively, are shown. The measured fringe spacing is a) $115 \pm 15\mu$m and c) $40 \pm 2\,\mu$m. This is in good agreement with theory where the fringe spacing is determined by the frequency difference between the chirped and anti-chirped spectra.

delay was continuously scanned by moving a motor with a velocity of $0.500 \pm 0.005\,\mathrm{mm/s}$ while the signal was recorded with a sample rate of 250 kHz. The SFG signal was detected within a bandwidth of 0.09 nm FWHM around $394.9 \pm 0.1\,\mathrm{nm}$. The entire data set took 7 s to accumulate with a resolution of about 100 points per fringe. The fringes in Figs. 4.4b) & d) for white-light and CPI have $87.1 \pm 0.2\,\%$ and $84.5 \pm 0.5\,\%$ visibility, respectively.

One can clearly see that the CPI fringe period, $395 \pm 4\,\mathrm{nm}$, is half that of the white light, $795 \pm 8\,\mathrm{nm}$, demonstrating phase super-resolution. The PSR signal in Fig. 4.4d) is centered around -500μm to show it free of residual white-light interference due to imperfect alignment. Comparing Figs. 4.4a) & c) we see another characteristic in our classical system often associated with quantum interference. The coherence length for the white-light interference pattern is $63.5 \pm 0.3\mu$m FWHM, in good agreement with expectations from the bandwidth of the chirped pulse of 10 nm FWHM at 790 nm. The width of the PSR interferogram, on the other hand, is approximately 5mm FWHM, a factor of 80 larger. Under ideal conditions, perfect mode overlap, matching chirp rates and bandwidths, and assuming Gaussian spectra, the width of the interferogram is calculated to be 19 mm, the length of the chirped pulses.

Phase super-resolution has previously been shown in a multiport classical interferometer in the coincidence rate between a set of photon counters [43]. The CPI approach demonstrated here is different in two important ways. It does not rely on single-photon detection facilitating rapid data accumulation. Furthermore, it is the first observation of a classical analogue to dramatically different one-photon and two-photon coherence lengths that have been reported in entangled quantum systems [51, 52].

4.4 Conclusion

We have shown classical analogues to three archetypical quantum interference effects by making modifications to chirped-pulse interferometry. This work demonstrates the first observation of classical analogue of the Hong-Ou-Mandel peak and quantum beating. We have also demonstrated a new method for observing phase super-resolution in a classical interferometer suitable for rapid data acquisition and exhibiting a coherence length much longer than that of the laser light. These results are a step toward answering a central

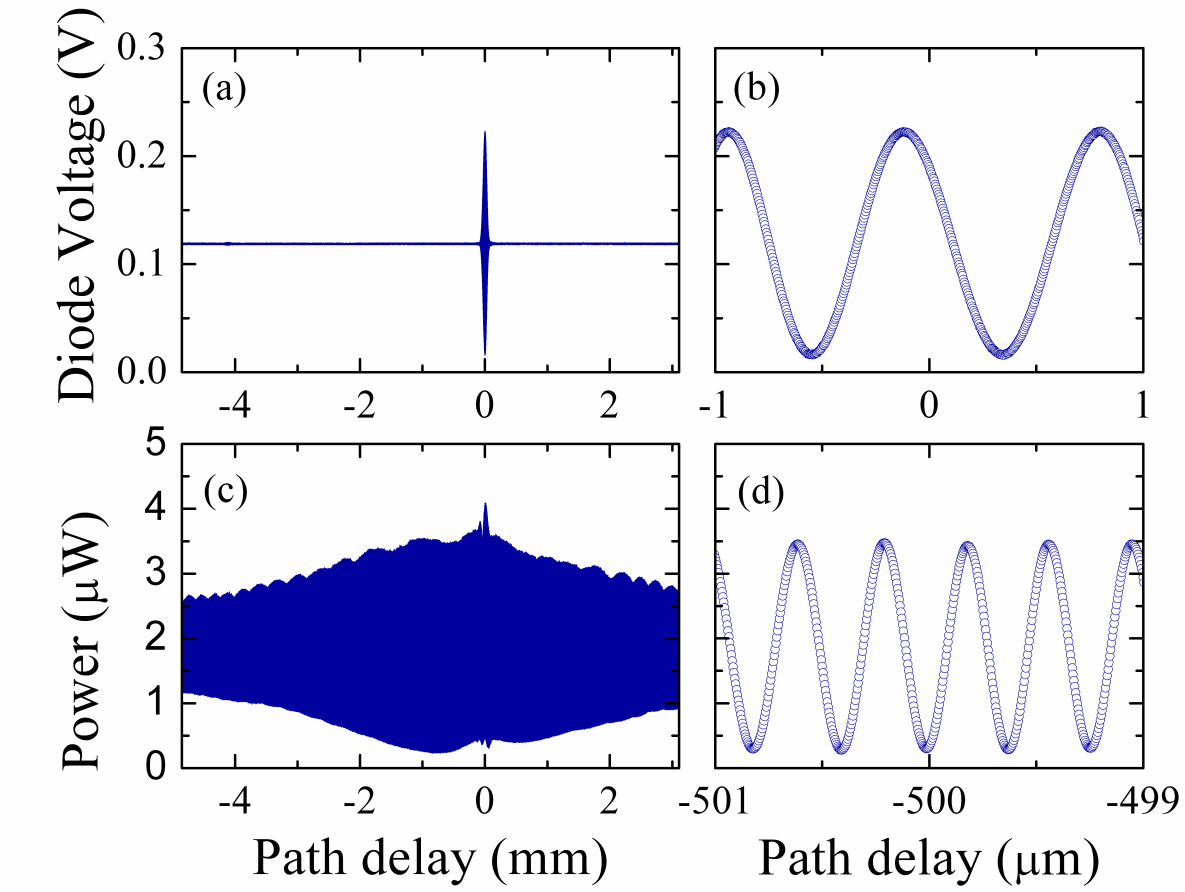

Figure 4.4: White-light interference pattern and phase super-resolution in CPI. a) & b) shows the white-light interference pattern generated by the chirped pulse. c) & d) show the SFG signal detected in the modified CPI depicted in Fig. 4.1c) (lower). By comparing b) & d) one can clearly see the reduction of the fringe wavelength in CPI; this is phase super-resolution. In addition, by comparing the signals in a) & c), we see that the CPI coherence length is roughly 80 times longer than the white-light coherence length.

question in quantum information science as to which phenomena require quantum resources and which can be achieved classically.

Chapter 5

Outlook

My Master's project aimed to develop Chirped-Pulse Interferometry (CPI), a new interferometry technique for precision time delay measurements. The interferometer uses ultrafast pulse stretching and compression techniques and nonlinear optics. The results of our approach demonstrated the same signatures and immunity to dispersion of two-photon HOM interferometry, based on quantum mechanically entangled photons, yet our approach requires no entanglement at all. The experimental results are very exciting for the fields of interferometry and quantum optics. The results show that one can gain all of the advantages of the quantum technique without the limitations of weak and experimentally complex entangled photon sources. Moreover, I have shown that by modifying CPI in analogous ways to the HOM interferometer, CPI can also be made to produce interferometric signal identical to the HOM peak, quantum beating, and phase super-resolution. CPI's demonstrated features make the technique very promising in the field of optical imaging. However, for the performance of CPI to compete with time-domain optical coherence tomography, some aspects of our previous approach would have to be improved.

The natural direction for future work consists of pushing further the technique of Chirped-Pulse Interferometry. The goal would be to image a real complex biological sample and make CPI a valuable and competitive technique compared to the standard non-invasive imaging technology. A possible approach differs substantially from our previous scheme. The use of a computer-controlled spatial light modulator to "shape" laser pulses instead of relying on grating-based stretcher and compressor will be advantageous. This will allow a greater degree of flexibility and control that is impossible when limited to grating-based

designs. The use of oppositely chirped pulses has a few disadvantages that can be eliminated using the modulator. This new design would enable us to increase the signal-to-noise ratio and improve the image quality.

The axial resolution of a complex sample is directly related to the spectral bandwidth of the source of light. For this reason, an ultra-short laser pulse should be used, with a spectral bandwidth several times broader than the previous source used for this thesis. The axial resolution will not be limited by the increased spectral bandwidth due to the inherent immunity to material dispersion. However, a compromise would have to be made between the acceptance bandwidth of the nonlinear crystal, and the signal power. A thinner crystal allows a wider range of frequency components to be phase matched, while the power conversion efficiency requires thicker crystals. Furthermore, high sensitivity photomultiplier tubes could replace the simple and inexpensive amplified photodiode used here, to better detect weak sum-frequency generation. Finally, a complete tomographic characterization of complex samples requires focusing elements that will have to be integrated, to direct the probing beam at the sample. It will lead to additional challenges, not encountered in my work, such that a compromise between the axial probing depth and the transverse resolution. Those improvements will lead to a high quality non-invasive imaging technique and surpass the common imaging techniques for biomedical applications.

Bibliography

[1] J.C. Diels and W. Rudolf, "Ultrashort laser pulse phenomena: Fundamentals, techniques, and applications on a femtosecond time scale," 2nd edition, Academic Press, Burlington, MA, 2006. 2, 5, 8, 12, 30

[2] E. B. Treacy, *Quantum Electron.* **QE-5**, 454 (1969). 6, 7, 8, 53

[3] D. Strickland and G. Mourou,"Compression of amplified chirped optical pulses," Opt. Commun. **56**, 219 (1985) 6

[4] O. E. Martìnez, "Matrix formalism for pulse compressors," IEEE J. Quantum Electron, **24**, 2530 (1988). 9, 53

[5] A. M. Weiner, "Femtosecond pulse shaping using spatial light modulators,"Rev. Sci. Instrum. **71**, 1929 (2000) 9

[6] O. E. Martìnez, "Negative group-velocity dispersion using refraction," J. Opt. Soc. Am. A, **1**, 10 (1984). 9

[7] R. W. Boyd, "Nonlinear optics,"2nd edition, Academic Press, San Diego, CA, 2003. 10, 11

[8] R. L. Sutherland, "Handbook of Nonlinear Optics," 2nd edition, CRC Press, New York, 2003. 11

[9] A. F. Abouraddy, M. B. Nasr, B. E. A. Saleh, A. V. Sergienko, and M. C. Teich, "Quantum-optical coherence tomography with dispersion cancellation," Phys. Rev. A **65**, 053817 (2002). 15, 16, 22, 23, 41, 43, 47, 49

[10] A. F. Fercher, W. Drexler, C. K. Hitzenberger, and T. Lasser, "Optical coherence tomography - principles and applications," Rep. Prog. Phys. **66**, 239-303 (2003). 16, 24, 41

[11] C. K. Hong, Z. Y. Ou, and L. Mandel, "Measurement of subpicosecond time intervals between two photons by interference," Phys. Rev. Lett. **59**, 2044-2046 (1987). 16, 24, 41, 52

[12] A. M. Steinberg, P. G. Kwiat, and R. Y. Chiao, "Dispersion cancellation in a measurement of the single-photon propagation velocity in glass," Phys. Rev. Lett. **68**, 2421-2424 (1992). 17, 18, 20, 22, 41, 52

[13] M. B. Nasr, B. E. A. Saleh, A. V. Sergienko, and M. C. Teich, "Demonstration of Dispersion-Canceled Quantum-Optical Coherence Tomography," Phys. Rev. Lett. **91**, 083601 (2003). 20, 41, 44

[14] K. Resch, R. Kaltenbaek, J. Lavoie, D. N. Biggerstaff, "Chirped-pulse interferometry with finite frequency correlations," Proc. SPIE, Vol. 7465, 74650N (2009) 30, 31

[15] J. Altepeter, E. Jeffreys, and P. Kwiat, "Phase-compensated ultra-bright source of entangled photons," Opt. Express **13**, 8951-8959 (2005). 36, 44

[16] R. Kaltenbaek, J. Lavoie, D. N. Biggerstaff, and K. J. Resch, "Quantum-inspired interferometry using chirped laser pulses," Nat. Phys. **4**, 864-868 (2008) 40, 41, 43, 50, 51

[17] J. G. Fujimoto, M. E. Brezinski, G. J. Tearney, S. A. Boppart, B. Bouma, M. R. Hee, J. F. Southern, and E. A. Swanson, "Optical biopsy and imaging using optical coherence tomography," Nature Med. **1**, 970-972 (1995). 41

[18] W. Drexler, "Ultrahigh-resolution optical coherence tomography," J. Biomed. Opt. **9**, 47-74 (2004). 41

[19] B. I. Erkmen and J. H. Shapiro, "Phase-conjugate optical coherence tomography," Phys. Rev. A **74**, 041601 (2006). 41

[20] K. Banaszek, A. S. Radunsky, and I. A. Walmsley, "Blind dispersion compensation for optical coherence tomography," Opt. Commun. **269**, 152-155 (2007). 41

[21] K. J. Resch, P. Puvanathasan, J. S. Lundeen, M. W. Mitchell, and K. Bizheva, "Classical dispersion-cancellation interferometry," Opt. Express **15**, 8797-8804 (2007). 41, 52

[22] M. Pessot, P. Maine, and G. Mourou, "1000 times expansion/compression of optical pulses for chirped pulse amplification," Opt. Commun. **62**, 419-421 (1987). 43

[23] Sellmeier coefficients, representative for Code 0211 microsheet glass, were provided by Corning Inc. 44

[24] If the bandwidth in HOM interference is determined by a pair of Gaussian bandpass filters in front of the detectors, rather than by the source, then the HOM dip is narrower than the WLI by only a factor of $\sqrt{2}$. 49

[25] S. Carrasco, M. B. Nasr, A. V. Sergienko, B. E. Saleh, M. C. Teich, J. P. Torres, and L. Torner, "Broadband light generation by noncollinear parametric downconversion" Opt. Lett. **31**, 253-255 (2006). 50

[26] A. Pe'er, Y. Bromberg, B. Dayan, Y. Silberberg, and A. A. Friesem, "Broadband sum-frequency generation as an efficient two-photon detector for optical tomography" Opt. Express **15**, 8760-8769 (2007). 50

[27] J. D. Franson, *Phys. Rev. A* **45**, 3126 (1992). 52

[28] C. Bonato et al., *Phys. Rev. Lett.* **101**, 233603 (2008). 52

[29] J. D. Franson, *Phys. Rev. Lett.* **62**, 2205 (1989). 52

[30] Z. Y. Ou, X. Y. Zou, L. J. Wang, and L. Mandel, Phys. Rev. Lett. 65, 321 (1990). 52

[31] T. B. Pittman, Y. H. Shih, D. V. Strekalov, and A. V. Sergienko, Phys. Rev. A 52, R3429 (1995). 52

[32] D. V. Strekalov, A. V. Sergienko, D. N. Klyshko, and Y. H. Shih, Phys. Rev. Lett. 74, 3600 (1995). 52

[33] J. G. Rarity et al., *Phys. Rev. Lett.* **65**, 1348 (1990). 52

[34] M. W. Mitchell, J. S. Lundeen, and A. M. Steinberg, *Nature* **429**, 161 (2004). 52

[35] P. Walther et al., *Nature* **429**, 158 (2004). 52

[36] B. Yurke, *Phys. Rev. Lett.* **56**, 1515 (1986). 52

[37] H. Lee, P. Kok, and J. P. Dowling, *J. Mod. Opt.* **49**, 2325 (2002). 52

[38] V. Giovannetti, S. Lloyd, and L. Maccone, *Science* **306**, 1330 (2004). 52

[39] B. L. Higgins et al., *Nature* **450**, 393 (2007). 52

[40] R. S. Bennink, S. J. Bentley, and R.W. Boyd, *Phys. Rev. Lett.* **89**, 113601 (2002). 52

[41] F. Ferri et al., *Phys. Rev. Lett.* **94**, 183602 (2005). 52

[42] J. Lavoie, R. Kaltenbaek, and K. J. Resch, *Optics Express* **17**, 2818 (2009). 52, 53

[43] K. J. Resch et al., *Phys. Rev. Lett.* **98**, 223601 (2007). 52, 53, 59

[44] K. Mattle, H. Weinfurter, P. G. Kwiat, and A. Zeilinger, Phys. Rev. Lett. 76, 4656 (1996). 52, 53

[45] Z. Y. Ou and L. Mandel, *Phys. Rev. Lett.* **61**, 54 (1988). 52, 53, 57

[46] T. Legero et al., *Phys. Rev. Lett.* **93**, 070503 (2004). 52, 53, 57

[47] C. H. Bennett et al., *Phys. Rev. Lett.* **70**, 1895 (1993). 52

[48] D. Bouwmeester et. al., *Nature* **390**, 575 (1997). 52

[49] E. Knill, R. Laflamme, and G. J. Milburn, *Nature* **409**, 46 (2001). 52

[50] K. J. Resch et al., *Phys. Rev. A* **69**, 063814 (2004). 54

[51] E. J. S. Fonseca, C. H. Monken, and S. Pádua, *Phys. Rev. Lett.* **82**, 2868 (1999). 59

[52] K. Edamatsu, R. Shimizu, and T. Itoh, *Phys. Rev. Lett.* **89**, 213601 (2002). 59